# 7 Pulsed Laser Deposition of ZnO-Based Thin Films

M. Lorenz

Pulsed laser deposition (PLD) is a growth method for thin films by condensation of a laser plasma ablated from a single target, excited by the high-energy laser pulses far from equilibrium. First, the PLD technique is briefly described beginning with the history and the fundamental processes. In the main part, the suitability of PLD as a fast and flexible exploratory research technique for high-quality ZnO-based thin film heterostructures is demonstrated by reviewing recent results. Finally, the innovative potential inherent to PLD will be demonstrated by mentioning advanced PLD techniques, including a high-pressure PLD process for free-standing ZnO-based nanowire arrays.

## 7.1 Brief History and Basics

Pulsed laser deposition (PLD) [1–3] uses high-power laser pulses with an energy density of more than $10^8\,\mathrm{W\,cm^{-2}}$ to melt, evaporate, excite, and ionize material from a single target. This laser ablation produces a transient, highly luminous plasma plume that expands rapidly away from the target surface. The ablated material is collected on an appropriately placed substrate surface upon which it condenses and a thin film nucleates and grows.

The first demonstration of PLD by Smith and Turner in 1965 was induced by the development of the ruby lasers [1]. The technique remained dormant for the next 20 years, and only about 100 PLD papers were published until 1986. The breakthrough of PLD as an accepted growth technique was made possible by the development of high-power lasers with sufficiently high pulse energy and short pulse length, i.e., gas lasers with high-power thyratron switches or Q-switched solid state lasers [4]. In addition, with the discovery of the high-$T_c$ oxide superconductors a complex oxide material of a high technological relevance was found [5, 6], which was very well suited for PLD. Concerning this, Dijkamp and Venkatesan demonstrated in 1987 the superior quality of $YBa_2Cu_3O_{7-\delta}$ films grown by PLD compared to those previously grown by other deposition methods [1]. The considerable research efforts concentrated in the 1990s on the high-$T_c$ superconductor thin films pushed the devolopment of the PLD in terms of reproducibility [2, 7, 8], scaling to larger substrate areas [9,10], and deposition of heterostructures and multilayers [11]. Present day, PLD is an established growth technique for a variety of

materials [12]. Advantages of PLD compared to other established techniques are as follows [2, 5]:

- The capability for stoichiometric transfer of multielement compounds from a single target to the substrate, i.e., the chemical composition of complex materials such as $YBa_2Cu_3O_{7-\delta}$ can be reproduced nearly unchanged in the deposited films. However, as will be shown later, exceptions from this general rule exist.
- PLD is a reliable, versatile, and fast process. The deposition rate is in the order of tens of $\mathrm{nm\,min^{-1}}$ on small substrate areas of $1\,\mathrm{cm^2}$. The film thickness can be easily controlled by the number of applied laser pulses.
- The laser as the external energy source for materials vaporization and the deposition chamber are spatially separated, resulting in an extremely clean process. The PLD process requires no filament or plasma gas inside the growth chamber as in contradiction thermal evaporation and sputtering do. Thus, an inert or reactive background gas can be applied during PLD growth with nearly no limitation of pressure, which can be controlled over orders of magnitude from the $10^{-5}$ mbar up to the 1 mbar range.
- The synthesis of metastable materials and the formation of films from species appearing only in the laser plasma are possible by PLD [2].

In spite of these advantages, industrial use of PLD has been slow [13] and nowadays there are only a few examples of smaller start-up companies using PLD for highly specialized applications [14–16]. Most PLD work up to now has been focused on the research field and the reasons for that are listed here:

- The volume deposition rate of PLD is only about $10^{-5}\,\mathrm{cm^3\,s^{-1}}$, that is much lower than that of other physical vapor deposition techniques as electron beam evaporation, magnetron sputtering, and vacuum arc deposition [17]. Furthermore, the energetical efficiency of high power lasers is only a few percent, which means that the overall efficiency of PLD is also low [18]. Consequently, upscaling of PLD to larger substrate areas is limited to about 5 in. diameter [9] due to the highly forward directed plasma plume [19]. Therefore, without additional lateral scanning of the substrate, a sufficiently good thickness and composition homogeneity of the deposited films is limited to an area of about $1\,\mathrm{cm^2}$.
- Depending on target density and material and on the deposition parameters, particulates and globules of molten material, the so called droplets, can be found on the deposited films [20]. The size of the droplets is typically in the 1 µm range. The droplets are detrimental for some film applications at the microscale, especially if lateral structuring in the micrometer range is required. For reduction or even suppression of the droplets, velocity filters, parallel off-axis configurations of plasma plume and substrate, and PLD setups with two colliding plasma plumes [21] have been used successfully. These additional precautions are based on

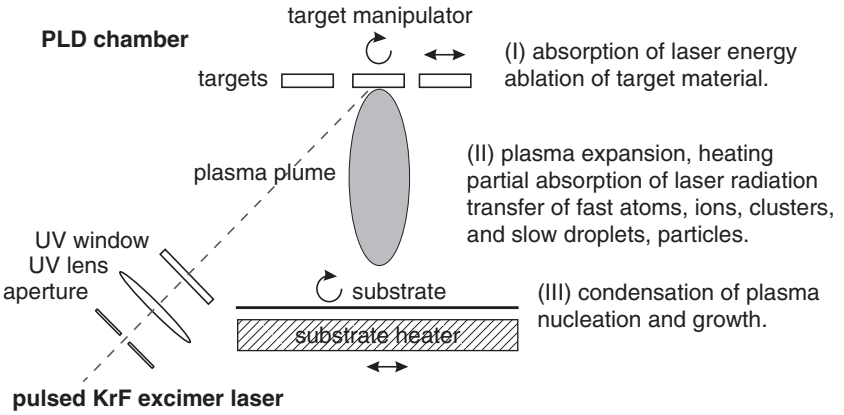


**Fig. 7.1.** Scheme of a typical PLD setup for large-area film growth. The main functional parts are designated on the *left*. The fundamental processes during (I) target ablation, (II) plasma expansion, and (III) growth are shortly described on the *right*, as introduction to the more detailed description in this section

the different expansion dynamics of the small and fast atoms and clusters and of the much heavier and slower particulates and droplets in the laser plasma. However, the droplet reduction techniques often reduce the deposition rate and make the process much more complicated [1, 5].

– The fundamental processes of PLD, the laser ablation of material, the plasma creation and expansion, and the film nucleation and growth (see Fig. 7.1), are not fully understood up to now [3, 22]. Modeling of these processes is difficult because of their strong nonequilibrium character due to the high pulse energy coupled with short laser pulse lengths of typically some 10 ns. Thus, deposition of novel materials usually requires a period of empirical optimization of the PLD parameters by close interaction of growth and immediate film characterization.

## 7.2 Fundamental Processes and Plasma Diagnostics

The success of PLD has far surpassed the understanding of the fundamental laser ablation processes for the usually used high laser energies and short pulse lengths. PLD involves a wide range of physical phenomena and their investigation requires expensive diagnostics with nano- or picosecond time resolution [23]. However, as stated already in Sect. 7.1, for the optimization of the growth of a particular thin film material, the detailed ablation mechanisms are of minor importance in many cases [2]. Relevant from a more practical viewpoint is that the ablation takes place on a short time scale in the nanosecond range to minimize the dissipation of the laser energy

beyond the volume of the melted and ablated surface layer of the target. Only within this condition, thermal destruction of the target together with phase segregation will be avoided. Furthermore, as well known as one of the major advantages of PLD and as mentioned earlier, the relative concentration of elemental species within the plasma plume corresponds to the chemical composition of the target material. Therefore, from this general consideration, PLD seems to be very well suited for the growth of granular crystalline or amorphous thin films with complex stoichiometry [2].

To give an overview on the very different basic effects occurring in PLD, the physical processes will be briefly reviewed in the following. Figure 7.1 shows schematically the main functional parts of a typical PLD setup and lists the fundamental processes during a PLD experiment. The phenomena during PLD can be divided into three main steps (I) ablation of the target material, (II) plasma expansion, and (III) condensation at the substrate surface [4, 24, 25]. Figure 7.2 shows a photograph of the inner parts of a PLD chamber suitable for large-area deposition up to 3-in. diameter as designed and built at the University Leipzig.

(I) *Absorption* of the laser energy and *ablation* of the target material. According to [26], the laser ablation (also called photon induced sputtering) can be classified into the following primary and secondary mechanisms that take place simultaneously. The share of each particular process is hardly to determine.

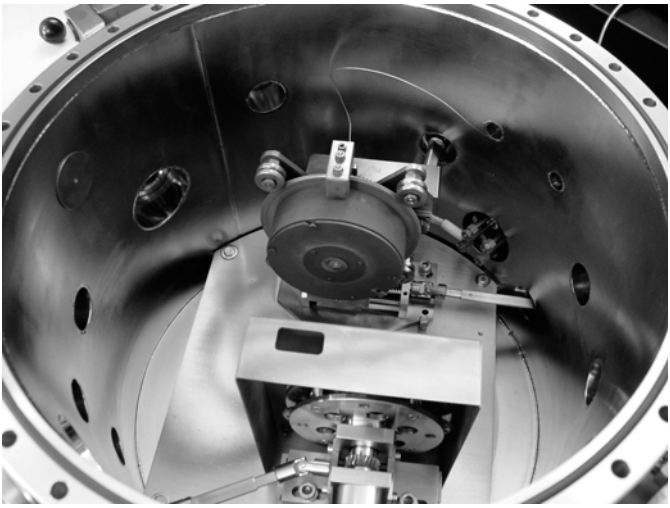

**Fig. 7.2.** View into a PLD chamber built at University Leipzig with inner diameter of 405 mm, compromising a target manipulator (in front), a 3-in. diameter heater with a rotatable holder for 1 $cm^2$ substrates (in the back). The laser entrance window into the chamber is visible left to the substrate heater. Compare Table 7.2 for technical details of this particular PLD chamber

- Thermal ablation by absorption of laser energy by the phonon system, melting, and evaporation of target material. The thermal sputtering can be described using the heat conduction equation, the thermodynamic materials parameters, the refractive indices (see [24]), and the laser parameters (wavelength, pulse duration, energy density). Beside evaporation, molten globules (droplets) can be expelled into the plasma by laser-induced recoil pressure or sub-surface superheating [20]. Such droplets can be found on the grown films as shown below in Fig. 7.13.
- Exfoliational sputtering occurs when flakes are detached from the target due to repeated thermal shocks. A high linear thermal expansion coefficient, a high Young's modulus, and a high melting point of the target material are necessary for exfoliational sputtering. In addition, the laser-induced temperature must approach, but not exceed the melting point to result in a shock wave induced cracking.
- Hydrodynamic sputtering means forming of droplets at the target as a result of transient melting and has no analog in ion sputtering. Asperities are formed at the target surface after melting.
- Nonthermal, photoinduced electronic sputtering is due to direct interaction of the laser photons with the electronic system of the target and involves for example photoablation, i.e., breaking of chemical bonds by high energy photons from the laser (5 eV at 248 nm wavelength). The photons can also create color centers that enhance thermal absorption of the target material [25].
- Indirect collisional sputtering of the target by photon generated secondary ions and electrons from the laser plasma results in cone formation and target erosion [27]. Another secondary process is heating of the target by the laser-generated plasma.

(II) *Expansion* of the laser plasma including transfer of material. The laser radiation is partly absorbed by the vaporized target material and thereby a heated and excited laser-induced plasma is produced. The main absorption processes are photoabsorption and inverse Bremsstrahlung. The absorption due to inverse Bremsstrahlung dominates for long laser wavelengths, e.g., $CO_2$-lasers with wavelength of 10.6 µm, and is of little importance for KrF excimer lasers with wavelength of 248 nm. The reflection loss is less than 1% for 248 nm laser wavelength [25]. The modeling of the plasma expansion and the material transfer from the target to the substrate sensitively depends on the background gas pressure during PLD growth [25]:

- Under high vacuum conditions, i.e., pressure $p < 10^{-2}$ mbar, the material transfer can be described using Monte Carlo simulations. Usually, inelastic collisions and collective phenomena as shock waves cannot be considered here. The so called Direct Simulation Monte Carlo method allows extension to slightly higher gas pressures.

- The hydrodynamic model is based on a sufficiently high collision probability under thermodynamic equilibrium. This condition is fulfilled only at $p > 1$ mbar, i.e., at high pressures above the typical PLD film deposition conditions, or at the beginning of plasma expansion, at high plasma density (small target to substrate distance).
- The model of an expanding shock wave according to Sedov and Taylor is valid at high pressures and large target-to-substrate distance.
- For the most important intermediate pressure range from $10^{-2}$ to 0.5 mbar exist only empirical friction models. In [25] an extension of the shock wave model is proposed, which is valid from $10^{-2}$ to 0.5 mbar at lower target-to-substrate distance from 20 to 50 mm.

The laser plume from a ZnO target was investigated experimentally [28, 29]. Time of flight and quadrupole mass spectrometry and photoionization has been used to study the mass, charge, and kinetic energy of species ejected from a ZnO target in dependence on the energy density of a KrF laser [28]. Mostly, monatomic Zn and O atoms and ions were found. The desorption and ablation thresholds for ZnO were determined to be 0.25 and 0.7 J cm$^{-2}$, respectively. Neutral Zn atoms had energies from 1 to 4 eV, whereas Zn ions had maximum energy above 100 eV [28]. The time evolution of the laser plume of ZnO during ablation with an ArF laser in He gas was investigated in [29]. A typical luminescence spectrum of the ZnO plume in He gas at 4 mbar pressure at 30 mm distance from the target comprises several peaks ranging from about 250 up to 680 nm optical wavelength, which were assigned to neutral excited Zn atoms.

(III) *Condensation* of material at the substrate surface, *nucleation* and *film growth*. In contrast to the very complex processes of plasma expansion and transfer of target material to the substrate, the nucleation and growth at the substrate surface can be described by models, which also apply for other physical vapor deposition methods, such as molecular beam epitaxy (MBE), sputtering, or ion beam deposition [25]. Even the pulsed nature of PLD does not modify the well known three-dimensional island (Volmer–Weber), two-dimensional full monolayer (Frank–van der Merwe), and two-dimensional monolayer growth followed by three-dimensional islands (Stranski–Krastanov) growth modes, if the growth rate per laser pulse is less than one molecular building block, i.e., less than about 2 Å per pulse [6]. For the growth of one atomic monolayer usually 5–10 laser pulses are required.

The growth kinetics describes the nucleation processes on the atomic scale. Thermally activated processes as adsorption, desorption, and diffusion at the surface and in the volume, nucleation, and crystallization/recrystallization determine the film structure and can be controlled by the substrate temperature and the growth rate. Using a diagram $\ln(R)$ over $1/T$, $R$ being the deposition rate and $T$ the growth temperature, three different growth modes (epitaxial, polycrystalline, and amorphous) can be

distinguished [30]. A similar structure zone model with the ratio of growth temperature to melting temperature and process pressure was already proposed by Thornton in 1977 for the sputtering of metallic films [4]. In addition to thermally dominated processes for energies <0.1 eV, atoms, ions, molecules, and clusters with higher kinetic energy between 0.1 and 1,000 eV are involved in PLD growth. Four specific cases can be distinguished, depending on the kinetic energy $E_{\mathrm{kin}}$ of the arriving particles in the laser plasma. The energy of the species depends on the laser energy density at the target and the background gas pressure together with the target–substrate distance [4, 25, 30]:

- For $E_{\mathrm{kin}} \cong 0.01-1$ eV, there is a thermal arrangement of particles, which dominates in MBE, laser-MBE [31], and electron beam evaporation.
- For $E_{\mathrm{kin}} \cong 0.2-50$ eV, surface penetration into the first monolayers reduces the temperature for epitaxy and yields a higher density of structures. These processes dominate in sputtering and PLD at higher background pressures of 0.05–0.5 mbar.
- For $E_{\mathrm{kin}} \cong 20-1{,}000$ eV, local deposition of energy creates vacancies and interstitials and local heating. Deposition far from equilibrium is typical for PLD at lower background pressure.
- For $E_{\mathrm{kin}} \cong 100\,\mathrm{eV}-10$ keV, sputtering of the solid state film surface probably can be element selective, and this reduces the growth rate of ion beam assisted processes and PLD.

## 7.3 PLD Instrumentation and Parameters for ZnO

The main parts of a PLD system are the high-power pulsed laser and the deposition chamber including laser optics. For the laser, usually excimer gas lasers or frequency multiplied solid state Nd-YAG lasers are used. Excimer lasers have the advantage of much higher pulse energy in the ultraviolet spectral range, which enables higher growth rates and large-area PLD up to 4-in. diameter. Table 7.1 compares the main parameters of a high-power excimer laser for research purposes of Coherent Lambda Physik [32] with that of a pulsed Nd:YAG solid state laser by Quantel [33]. In contrast with excimer lasers with maximum pulse energy of 1,200 mJ at 248 nm wavelength [32], frequency multiplied solid state lasers reach maximum pulse energies of about 500 mJ at 355 nm wavelength and only about 150 mJ at 266 nm [33]. Consequently, the less expensive solid state lasers are suitable only for PLD of small area films and most PLD groups use excimer lasers.

The second main part of a PLD system is the vacuum chamber. The author's group developed a large-area PLD process for the double-sided deposition of high-$T_c$ superconducting thin films (see for example [8, 10]). As substrate heater an arrangement of KANTHAL wire in ceramic tubes is used

**Table 7.1.** Comparison of main parameters of an excimer laser Coherent Lambda Physik LPX 305iF [32], and of a pulsed solid state Nd:YAG laser Quantel YG 981E [33], both suitable for research PLD systems

| Parameter | Excimer LPX 305iF | Pulsed Nd:YAG YG981E |
|---|---|---|
| Laser medium | KrF or ArF gas | Nd:YAG solid state |
| Basic wavelength | 248 or 193 nm | 1,064 nm |
| Maximum pulse energy | 1,200 mJ @ 248 nm | 1,600 mJ @ 1,064 nm |
| Harmonic wavelengths | – | 532, 355, 266 nm |
| Max. pulse energy at shorter wavelength | 650 mJ @ 193 nm | 490 mJ @ 355 nm & 150 mJ @ 266 nm |
| Maximum repetition rate | 50 Hz | 10 Hz |
| Maximum average power | 50 W @ 248 nm | n.a. |
| Pulse duration | 25 ns | 8–11 ns |
| Pulse-to-pulse stability | ±3% | ±2% (1,064 nm), ±8% (266 nm) |
| Beam dimensions | $12 \times 30\,\mathrm{mm}^2 (V \times H)$ | 9 mm diameter |
| Beam divergence | $1 \times 3$ mrad $(V \times H)$ | <0.5 mrad |
| Time jitter | ±2.5 ns | ±0.5 ns |

The initial investment cost of the Nd:YAG is less than half that of the excimer laser

(patent pending DE 10255453.7), which is suitable for double-sided deposition of double-side polished sapphire wafers. The main features of such a PLD chamber developed and built at University Leipzig are listed in Table 7.2. This PLD chamber with in situ ellipsometer ports is shown together with two other PLD chambers and the excimer laser LPX 305 in Fig. 7.3. In the last years, highly developed PLD and laser MBE chambers and systems with in situ reflection high-energy electron diffraction (RHEED, see Sect. 7.6.1) became available commercially [34–40]. Some of these developments are spin-offs of PLD-based research groups, i.e., of T. Venkatesan at University of Maryland (USA) [34], H. Rogalla and D. Blank at University Twente (Netherlands) [35], and H. Koinuma and M. Kawasaki from Tokyo Institute of Technology and Tohuku University Sendai (Japan), respectively [36], and of James A. Greer [37]. Thus, these PLD systems represent the highest available standard of research experience.

The typical parameters for the PLD of epitaxial ZnO-based thin films on sapphire including information about target preparation are listed in Table 7.3. Within the range of these software controlled parameters, the properties of the deposited films differ widely, as will be shown in Sect. 7.4. Beside the parameters listed in Table 7.3, the film properties will be influenced furthermore by a few more internal effects, which will be listed and discussed in the following according to the scheme effect/problem–cause–solution. Only the careful consideration of all these hidden effects by experienced operators can ensure the highest quality and reproducibility of PLD grown films.

**Table 7.2.** Main features of a PLD chamber for large-area substrates up to 3-in. diameter

| Parameter | Value |
|---|---|
| Inner diameter × height | $405 \times 335\,\mathrm{mm}^2$ |
| Number of Cu-sealed ports | 18 ports |
| Number of viton-sealed ports | 2 ports |
| In situ ellipsometer ports | 2 ports, angle of incidence 70° |
| Turbomolecular-drag-pump | $260\,\mathrm{l\,s}^{-1}$ |
| Base pressure | $1 \times 10^{-7}$ mbar |
| Gas inlet | 0–5,000 sccm |
| Background gas pressure | $10^{-5}$ to 10 mbar |
| Laser focusing lens | UV fused silica uncoated, $f = 300$ mm |
| Laser entrance window | UV fused silica uncoated, diameter $50 \times 5\,\mathrm{mm}^2$ |
| Target manipulator | 4 targets, max. diameter 25 mm, rotation and lateral translation |
| Target-to-substrate distance | 90–110 mm |
| Heater temperature | Max. 950°C |
| Substrate temperature | Max. 800°C |
| Substrate holder | One wafer up to 3-in. diameter |
| Substrate movement | Rotation and lateral offset |
| Computer control | Laser, gas pressure, heater, target, up to 11 consecutive steps |

The chamber was designed by D. Natusch, University Leipzig (Figs. 7.2 and 7.3) and the process control software was written by H. Hochmuth

- Accuracy and reproducibility of laser pulse energy – depending on how the laser pulse energy is controlled, for example the state of laser resonator windows may influence the obtained pulse energy values – regular cleaning of laser resonator windows.
- Deposition of the laser entrance window in the PLD chamber – reduced laser pulse energy – regular cleaning of the chamber entrance window after every growth run, shields between plume and window.
- Ablation state of target – the deeper the ablation crater in the target is, the more the direction of plume expansion swings around the target normal – use of new and large-area targets.
- Memory effects of previously deposited material – contamination of deposited film by material previously deposited in the chamber – use chamber only for one material, regular cleaning of all inner chamber parts.
- Evaporation of heater material at high temperature and low pressure – contamination of the grown film by material from the heater (see also Table 7.8) – use only high-temperature stable material for the hot parts of the heater.

**Fig. 7.3.** View into the PLD lab of the author in the Semiconductor Physics Group (head M. Grundmann) at University Leipzig, with three PLD chambers, excimer laser Lambda Physik LPX 305, and optical laser beam guiding system inside protection shielding. Two more PLD chambers are in the neighboring lab to the right

**Table 7.3.** Typical PLD parameters for epitaxial ZnO-based thin films, using an excimer laser LPX 305 (see Table 7.1), and the PLD chamber described in Table 7.2

| PLD parameter | Value |
|---|---|
| Background gases | $O_2$, $N_2$, $N_2O$ |
| Background gas pressure | $10^{-5}$ to 2 mbar |
| Laser pulse energy | 600 mJ |
| Mask at laser exit | $24 \times 10\,mm^2$ |
| Lens–target distance | Lens focus length plus 0–40 mm |
| Laser focus size at target | $5 \times 1.2$ to $9 \times 2.5\,mm^2$ depending on lens position |
| Laser energy density | 5–1.3 J $cm^{-2}$ depending on lens position |
| Target–substrate distance | 50–100 mm |
| Substrates | *c*-, *a*-, or *r*-plane sapphire, Si, SiC |
| Substrate temperature | 300–750°C |
| Target material | ZnO powder Alfa Aesar 99.9995% purity |
| Target preparation | Pressing, sintering @ 900–1,150°C for 12 h in air |
| ZnO film growth rate | 20–50 nm $min^{-1}$ @ 10 Hz pulse repetition rate |
| Film thickness | 2 nm to 2.5 µm |

## 7.4 Results on Epitaxial PLD ZnO Thin Films

This section describes the potential of PLD to grow high quality epitaxial ZnO-based thin films mainly on sapphire substrates , and in addition on silicon. Sapphire was chosen as the main substrate material because it fits sufficiently well the hexagonal structure of ZnO. The lattice mismatch of ZnO(0001) grown 30° in-plane rotated on sapphire(0001) is about 18%. As shown below, on *c*-plane and *a*-plane sapphire relaxed, granular ZnO thin films with thickness of a few 100 nm and very good in-plane orientation can be grown. Furthermore, sapphire single crystals are chemically stable in air, hard and available reasonably priced also for larger areas. Substrates with zero or 0.09% [22] lattice mismatch as ZnO or $ScAlMgO_4$ (SCAM), respectively, are a factor of 10–20 more expensive than sapphire. As will be shown in Sect. 7.5.4, ZnO thin films with superior performance have been grown on SCAM single crystals by the Kawasaki group in Sendai. However, up to 2005, SCAM substrates were not freely disposable outside Japan. Of course, ZnO can be grown by PLD also on other substrates as for example GaAs, Si, 3C-SiC buffered Si, 6H-SiC. However, because of the oxidizing growth regime of the ZnO PLD, the surface of Si and SiC templates tends to oxidize and the resulting amorphous $SiO_2$ layer prevents epitaxial ZnO growth and only *c*-axis textured ZnO films without in-plane orientation can be prepared (see Sect. 7.5.4). A more extensive table of substrates used for the PLD of ZnO is given in the review paper entitled "Pulsed laser deposition of thin films and superlattices based on ZnO" by Ohtomo et al. [22]. Beside this paper, there has recently been published a considerable number of extensive general or specialized reviews on ZnO, i.e., "A comprehensive review of ZnO materials and devices" by Özgür [41], "Epitaxial growth of ZnO films" by Tribulet [42], "P-type doping and devices based on ZnO" by Look [43], "Ferromagnetism of ZnO and GaN: A Review" by Liu [44], and a contribution to an Encyclopedia by Yao [45]. Because ZnO is a material with long-term research tradition with periodically increasing interest, the reader may compare also the older review of Hirschwald et al. [46].

In Sects. 7.4 and 7.5, we demonstrate the unique flexibility of PLD in growing high-quality ZnO-based thin films and heterostructures by presenting structural, electrical, optical, and device-related results of the Leipzig Semiconductor Physics Group headed by Marius Grundmann. More state of the art results of p-type and n-type conducting PLD ZnO films on various substrates are reviewed in Sect. 7.5.4. An overview on advanced PLD techniques offering extended possibilities in materials research is given in Sect. 7.6. Finally in Sect. 7.6.2, an innovative high-pressure PLD process for preparing ZnO-based nanostructures is demonstrated.

### 7.4.1 Structure of Nominally Undoped PLD ZnO Thin Films

The structure of the PLD grown ZnO thin films on *c*-plane, *a*-plane, and *r*-plane sapphire substrates will be explained by results of X-ray diffraction (XRD), transmission electron microscopy (TEM) with selected area diffraction patterns (SAD), and reflection high-energy electron diffraction (RHEED).

Figure 7.4 shows XRD $2\theta$-$\omega$ scans measured in Bragg–Brentano geometry with Ni-filtered Cu-$K_\alpha$ radiation on a Philips X'pert diffractometer with standard collimators and slits. Note the logarithmic intensity scaling in Fig. 7.4 which enhances the low-intensity background peaks as indicated. It is clearly seen that on *c*- and *a*-sapphire ZnO films grow with their *c*-axis perpendicular to the substrate surface, and on *r*-plane sapphire with an *a*-axis perpendicular to the substrate surface. Therefore, on *r*-plane sapphire the ZnO *c*-axis is in-plane of the surface. More detailed high-resolution X-ray analysis of PLD grown ZnO thin films has been done by Rahm [47].

Table 7.4 summarizes the out-of-plane and in-plane epitaxial relationships of ZnO films and sapphire substrates, the *c*-axis and *a*-axis lattice constants of ZnO, the ZnO full peak widths at half maximum (FWHM) of $2\theta$-$\omega$ and $\omega$ scans, and the tilt of the ZnO structure along surface normal [47]. Because of the low intensity of the asymmetric $(10\bar{1}4)$ reflection, the *a*-lattice constant has larger uncertainty compared to the *c*-axis lattice constant. The epitaxial relationships correspond to the results of Ohtomo (see Table 1 in [22]).

The microscopic structure of the PLD ZnO thin films and their interfaces to the sapphire or silicon substrates was investigated by TEM and HRTEM. Figure 7.5 shows a high resolution TEM cross-section of a nominally undoped ZnO thin film grown on *c*-plane sapphire. The epitaxial growth of the ZnO on the *c*-plane sapphire substrate is obvious and the interface layer is only about two monolayers thin. Figure 7.6 shows bright field TEM cross-section pictures of two epitaxial ZnO thin films grown at about 600°C at different oxygen partial pressure. Prior to the ZnO film, a laterally homogeneous, about 10 nm thick and single crystalline MgO buffer layer was grown, which acts as diffusion barrier as proved in Sect. 7.4.3. Figure 7.6a nicely shows the decreasing density of dislocation lines in the ZnO film from the interface to the film surface due to relaxation of the lattice misfit. For the ZnO films on MgO-buffered *c*-plane sapphire as shown in Fig. 7.6, the orientational relationship along growth direction is $[0001]_{\mathrm{ZnO}} \parallel [111]_{\mathrm{MgO}} \parallel [0001]_{\mathrm{sapphire}}$ and in-plane $[01\bar{1}0]_{\mathrm{ZnO}} \parallel [112]_{\mathrm{MgO}} \parallel [\bar{2}110]_{\mathrm{sapphire}}$ [48].

Figure 7.7 shows TEM and HRTEM images, partly together with the corresponding SAD patterns, of PLD ZnO films grown on Si(111) substrates [49]. Note that the lateral SAD image of the film on Si(111) was taken from many columns as indicated in Fig. 7.7a. The ZnO columns on Si(111) (and also on Si(100), see [49]) show no preferential azimuthal in-plane orientation relating to the Si substrate. Figure 7.7b shows a HRTEM lattice image with intermediate amorphous $SiO_x$ layer of 2–4 nm thickness and an additional interdiffusion

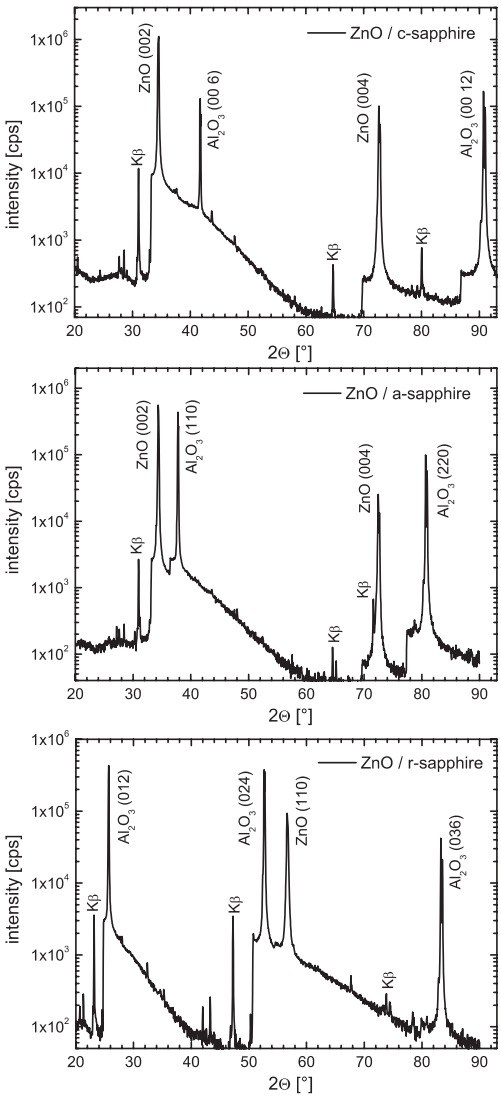


**Fig. 7.4.** XRD $2\theta - \omega$ scans of PLD grown, nominally undoped ZnO thin films on $c$-plane (*top*), $a$-plane (*center*), and $r$-plane (*bottom*) sapphire substrates, measured with Ni-filtered Cu-$K_\alpha$ radiation. The ZnO films were grown at 0.01 mbar $O_2$ and about 650°C

zone of silicon suboxides with the first ZnO monolayers. Figure 7.7c is a bright field (110)Si TEM cross-section of ZnO on Si(111). The intermediate $SiO_x$ interface layer is clearly visible again. The existence of this layer between the substrate and the actual thin film is most probably the reason for the very similar polycrystalline structure of the ZnO thin films grown on Si(111) and on Si(100) substrates.

**Table 7.4.** Results of high-resolution XRD analysis of several series of epitaxial PLD ZnO thin films grown on *c*-plane, *a*-plane, and *r*-plane sapphire at about 650°C substrate temperature, taken from [47]

| Parameter | | *c*-Sapphire | *a*-Sapphire | *r*-Sapphire |
|---|---|---|---|---|
| Epitaxial relations | ⊥ surface | (0001)‖(0001) | (0001)‖(11$\bar{2}$0) | (11$\bar{2}$0)‖(01$\bar{1}$2) |
| ZnO/sapphire | in-plane | [10$\bar{1}$0]‖[2$\bar{1}\bar{1}$0] | [11$\bar{2}$0]‖[0001] | [0001]‖[0$\bar{1}$11] |
| Lattice constants | *c* (Å) | 5.204 | 5.205 | Not measured |
| | *a* (Å) | 3.244 | 3.251 | 3.254 |
| FWHM | 2$\theta$ (°) | 0.012–0.027 | 0.012–0.015 | Not measured |
| ZnO(0002) | $\omega$ (°) | 0.042–0.128 | 0.061–0.079 | Not measured |
| Tilt along | (°) | None | None | 0.34 |
| Surface normal | | | | |

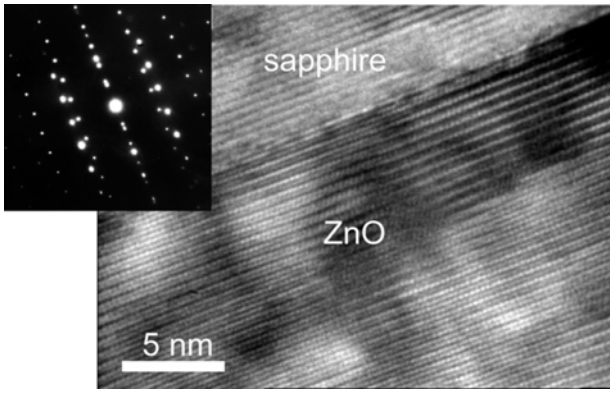


**Fig. 7.5.** High-resolution TEM cross section micrograph of a nominally undoped ZnO thin film on *c*-plane sapphire, PLD grown at 0.05 mbar $O_2$ and 700°C. The SAD pattern is taken from both film and substrate area. Images by G. Wagner, Leipzig

Figure 7.8 shows a ZnO film deposited on 3C-SiC buffered Si(111). The CVD-grown, only 3 nm thin 3C-SiC buffer layer does not improve the in-plane orientation of ZnO on Si. As already demonstrated in Fig. 7.7, polycrystalline ZnO without any preferential in-plane orientation was found. The HRTEM inset in Fig. 7.8 shows an amorphous layer at the ZnO/3C-SiC interface, which is formed by oxidation of the CVD grown 3C-SiC film. Interestingly, these ZnO films on SiC-buffered Si are *c*-axis textured and show slightly improved PL and CL characteristics compared to ZnO grown directly on silicon [50].

Figure 7.9 shows RHEED patterns obtained with 30 keV electrons impinging on clean surfaces of optimized ZnO thin films grown on *r*-, *a*-, and *c*-plane sapphire. The azimuthal directions of the two types of RHEED images of the *c*-axis oriented ZnO films (on *a*- and *c*-sapphire) are [1$\bar{1}$00] (top) and [$\bar{2}$110] (bottom) [52].

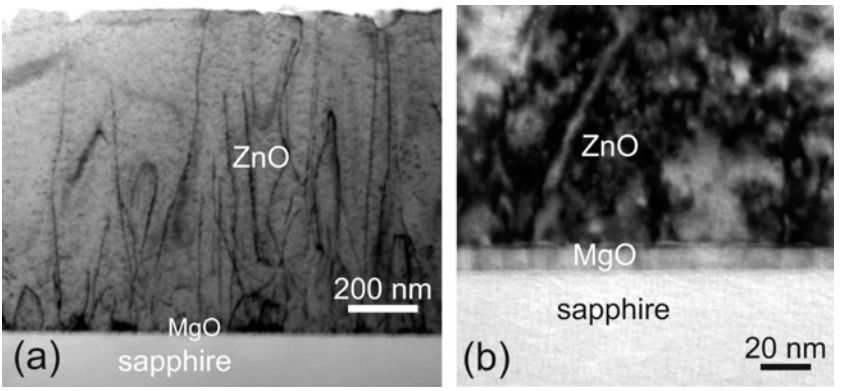


**Fig. 7.6.** TEM cross-sections of PLD ZnO thin films grown on MgO buffered *c*-plane sapphire. (**a**) ZnO was grown at 0.016 mbar $O_2$ and 600°C and shows decreasing density of dislocation lines from interface to surface. (**b**) ZnO was grown at $8 \times 10^{-4}$ mbar $O_2$ and 580°C. The thickness of the MgO buffer layer is about 10 nm. Images by W. Mader, Bonn

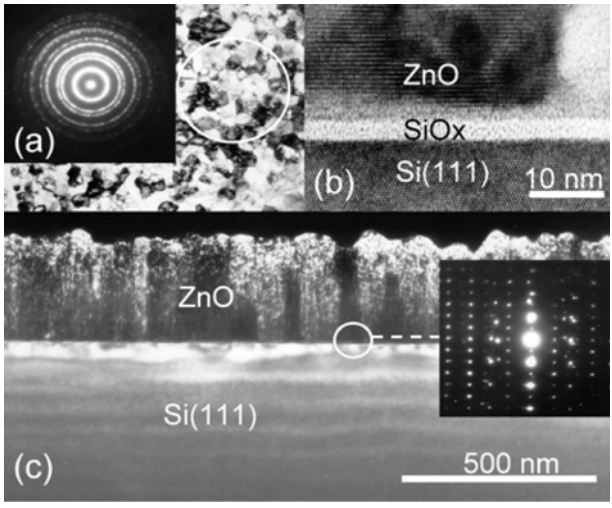


**Fig. 7.7.** TEM images and SAD patterns (*insets*) of a polycrystalline ZnO film on silicon (111) PLD grown at $1 \times 10^{-3}$ mbar $O_2$ and about 540°C: (**a**) Bright field Si(111) plane view observation, grain size is about 70 nm, (**b**) cross-section HRTEM lattice image with intermediate $SiO_x$ layer, and (**c**) weak beam Si(110) TEM cross-section. The area from which the SAD patterns were taken are within the *white circles*. Reprinted with permission from [49]

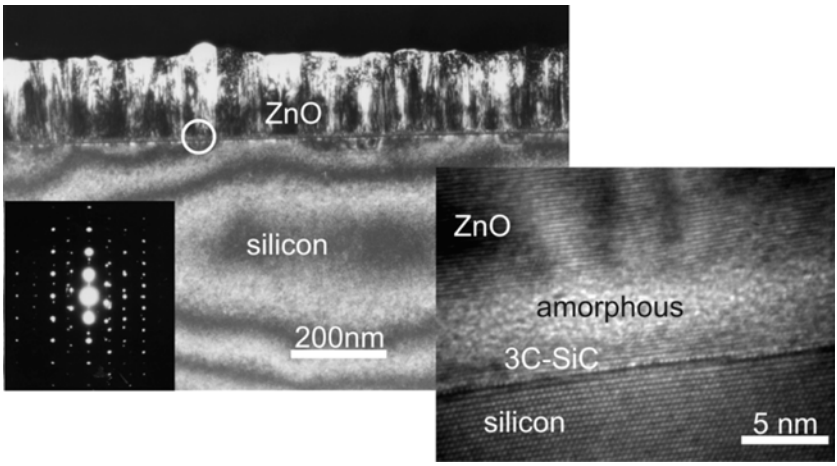


**Fig. 7.8.** TEM cross-section of an undoped PLD ZnO thin film on 3C-SiC buffered Si(111), grown at 0.016 mbar $O_2$ and 620°C. The SAD pattern (*inset*) was taken from the *circled area*. The HRTEM image (*right*) of the interface shows residual 3C-SiC and an amorphous interface layer. Images by G. Wagner, Leipzig

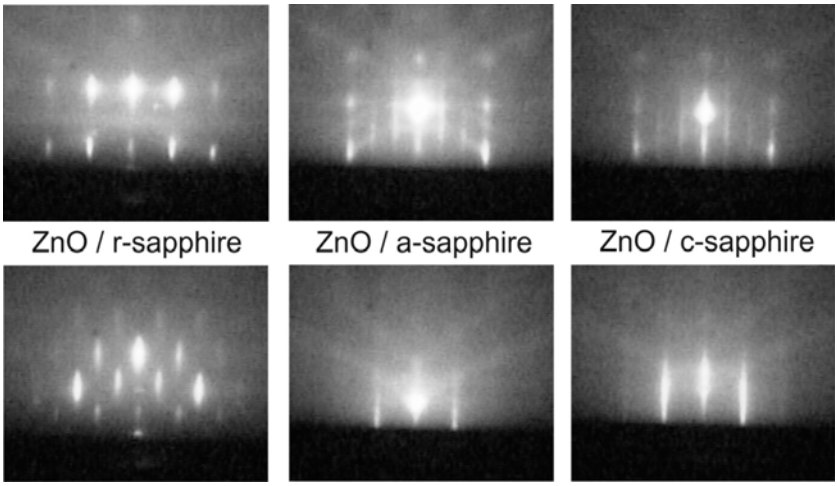


**Fig. 7.9.** RHEED images of optimized ZnO thin film surfaces on *r*-plane, *a*-plane, and *c*-plane sapphire, in the two azimuthal orientations (*top and bottom*) separated by 45° (*left*) or 30° (*middle and right*), respectively. The RHEED patterns of the *a*-axis textured film on *r*-plane sapphire (*left*) indicate an epitaxial and three-dimensional, island-like growth. The ZnO films on *a*-plane (*middle*) and *c*-plane sapphire (*right*) exhibit a smoother surface structure, as indicated by the streaky RHEED patterns and the observation of additional weak reflections in the *top* images due to $3 \times 3$ surface reconstruction [51]

### 7.4.2 Surface Morphology of PLD ZnO Thin Films

The surface morphology of the PLD grown ZnO-based films is important for the interface quality of multilayer structures, including quantum wells with thickness of a few nanometer only, for the formation of metal–semiconductor Schottky contacts and for the optical emission properties. Therefore, the control and optimization of surface properties is essential for the successful application of ZnO thin films in related device configurations.

Figure 7.10 shows the surface roughness of ZnMgO films deposited from a ZnMgO target with 4 wt. % MgO on *a*-plane sapphire substrates in dependence on the oxygen partial pressure during PLD. These investigations were done in view of optimization of ZnMgO/ZnO/ZnMgO quantum well structures (see Sect. 7.5.2), where indications for confinement effects were found in photoluminescence spectra [53]. Figure 7.10 shows minimum average roughness around 0.58 nm for $1 \times 10^{-3}$ mbar oxygen partial pressure. Figure 7.11 shows AFM images of roughness optimized ZnO, ZnMgO (deposited from ZnO:4 wt. % MgO target on ZnO buffer layer), and MgO thin films. The granular structure of all of these films is obvious with decreasing grain size from ZnO on top to MgO on the bottom.

ZnO films optimized for superior electrical properties as for example high Hall mobility at room temperature show increased roughness as shown in Fig. 7.12. As a general observation, many granular oxide thin film materials with optimized electrical or optical performance do not show low surface roughness simultaneously. Here, the mobility correlates with the grain size of the films because of the limiting effect of the grain boundary scattering, as

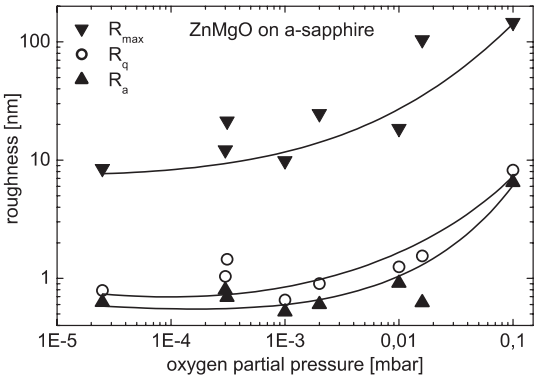


**Fig. 7.10.** Maximum, root mean square, and average roughness $R_{\max}$, $R_{\mathrm{q}}$, and $R_{\mathrm{a}}$, respectively (derived from $10 \times 10\,\mu\mathrm{m}^2$ AFM scans) of 300 nm thick ZnMgO films (PLD from a ZnO:4 wt. % MgO target) on *a*-plane sapphire in dependence on oxygen partial pressure during PLD growth. Lowest film surface roughness is obtained around $10^{-3}$ mbar. The lines are drawn to guide the eye. Measured by G. Zimmermann

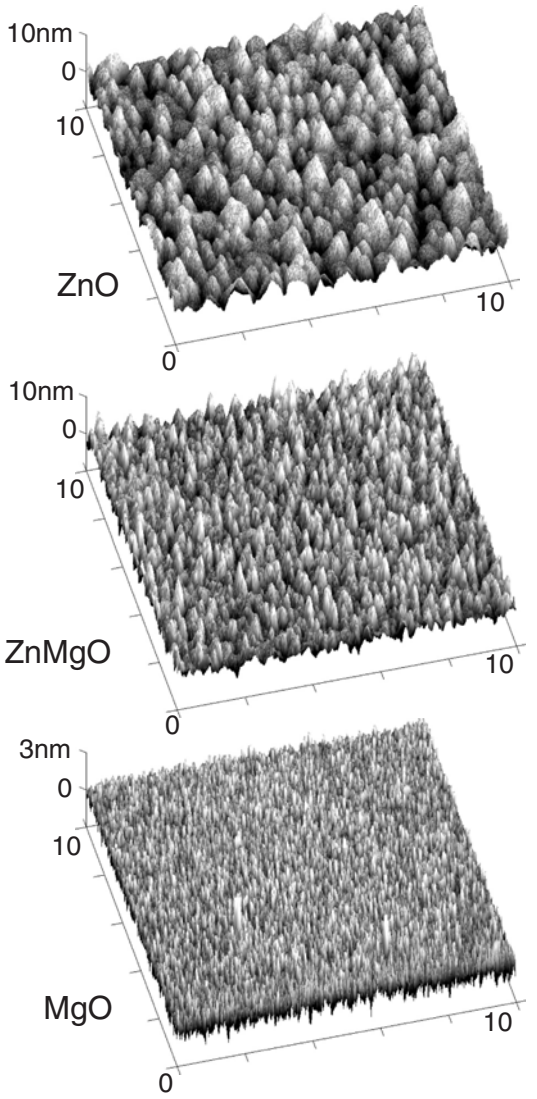


**Fig. 7.11.** AFM scan images ($10 \times 10\,\mu m^2$) of roughness optimized ZnO (*top*, 1.4 µm thick), ZnO:4 wt. % MgO (*center*, 250 nm thick on ZnO buffer), and MgO (*bottom*, 400 nm thick) films on *a*-plane sapphire with average roughness $R_a$ of 1.45, 0.41, and 1.23 nm, respectively. Measured by G. Zimmermann

shown already in [51]. The hexagonal wurtzite structure of the ZnO grains is clearly visible in Fig. 7.12.

The surface morphology of ZnO films on sapphire, 3C-SiC/Si, and 6H-SiC substrates was also investigated by scanning electron microscopy (SEM) as

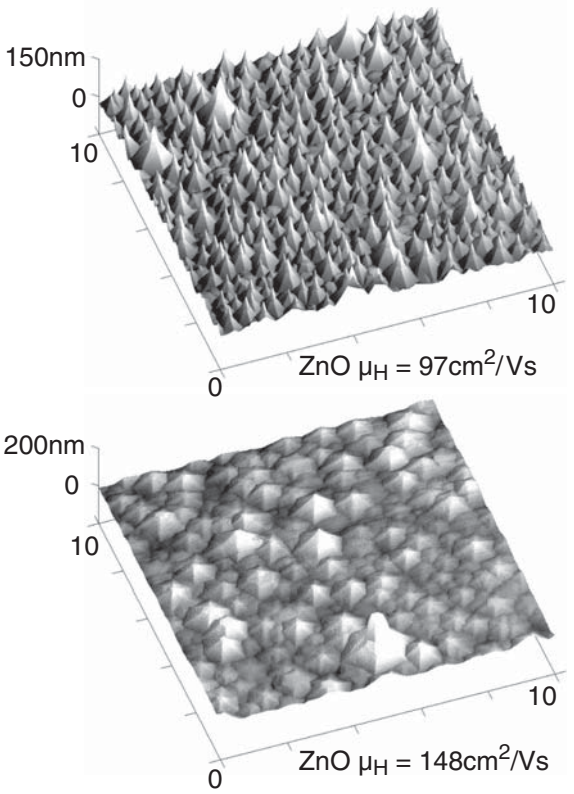


**Fig. 7.12.** AFM scan images ($10 \times 10\,\mu m^2$) of mobility optimized, $1.4\,\mu m$ thick ZnO thin films on *a*-plane sapphire. The Hall mobility at 300 K correlates with the grain size. The average roughness and the carrier concentration are $12.5\,nm/1.6 \times 10^{16}\,cm^{-3}$ (*top*) and $8.38\,nm/3.1 \times 10^{16}\,cm^{-3}$ (*bottom*), respectively. Measured by G. Zimmermann

shown in Fig. 7.13. The surface of an epitaxial ZnO film on *a*-plane sapphire appears very smooth without any structure, except the single larger particle visible in Fig. 7.13a. Figure 7.13b shows a textured ZnO film grown on 3C-SiC ($3\,\mu m$)/Si(100) without visible crack formation, however with larger hill-like structure with diameter of several micrometer in the center and many surface crystallites in the 100 nm range. Because of the increased lattice deformation of ZnO on single crystalline 6H-SiC substrates (see [54]), microcracks are obvious at the ZnO surface in Fig. 7.13c,d. At higher substrate temperature, some droplet-like particles are collected at these cracks (Fig. 7.13d).

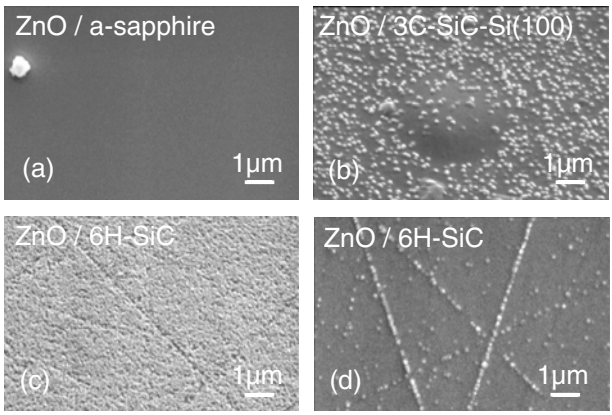


**Fig. 7.13.** Typical SEM images of PLD ZnO film surfaces: (**a**) ZnO (400 nm) on *a*-plane sapphire grown at 700°C, (**b**) ZnO (600 nm) on 3C-SiC (3 µm)/Si(100) grown at 640°C, (**c**) ZnO (300 nm) on 6H-SiC grown at 580°C, (**d**) ZnO (300 nm) on 6H-SiC grown at 700°C [54]

### 7.4.3 Electrical Properties of PLD ZnO Thin Films: Effect of Buffer Layers

The PLD grown ZnO-based films on sapphire can be arranged as follows according to their growth- and doping-dependent electrical performance [55], for references giving details about the particular PLD ZnO films see Table 7.9:

(a) Intrinsically n-type doped ZnO films deposited under various oxygen partial pressures show typical free electron concentrations from $10^{16}$ to $10^{18}\,\mathrm{cm}^{-3}$. Under particular deposition conditions, a low-temperature grown, thin ZnO nucleation layer may improve the electron mobility of the ZnO films on *c*- and *a*-plane sapphire.
(b) Unintentionally doped ZnO films prepared at high growth temperatures exhibit Al indiffusion from the sapphire ($Al_2O_3$) substrate, resulting in a background electron concentration of about $10^{16}\,\mathrm{cm}^{-3}$.
(c) Clean ZnO films with a $CeO_2$ or MgO diffusion barrier layer to supress the Al diffusion from the substrate. Semiinsulating behavior with a low electron concentration $\leq 10^{14}\,\mathrm{cm}^{-3}$ was obtained. In addition, also ZnMgO or ZnMnO films with more than 5 at. % Mg or more than 2 at. % Mn, respectively, show semi-insulating behavior.
(d) Intentionally doped ZnO layers with Ga or Al concentration up to a few at. % show electron concentrations above $10^{20}\,\mathrm{cm}^{-3}$, which is suitable for transparent conducting oxide (TCO) layers.
(e) Attempts for p-type conducting films by deposition in $N_2O$ background gas, by codoping with $N_2O$ and Ga, by doping with Li and N, and by group-V elements as Sb or P. A high Ga concentration up to $10^{19}\,\mathrm{cm}^{-3}$

could be compensated by codoping with $N_2O$, resulting in a semi-insulating behavior $\leq 10^{14}\,\mathrm{cm}^{-3}$, thus proving the acceptor-like incorporation of N in ZnO. Very low conductivity at the detection limit was obtained also for Li and P-doped films, partially enhanced by post deposition annealing, but up to now no clear indication for p-type conductivity was obtained.

Figure 7.14 depicts the ranges of resistivity vs. n-type carrier concentration of undoped and doped PLD ZnO thin films on sapphire [56]. A six orders of magnitude range of carrier concentration and resistivity ($2\times10^{14}$ to $2\times10^{20}\,\mathrm{cm}^{-3}$ and $10^{-3}$ to $10^{3}\,\Omega\,\mathrm{cm}$, respectively) could be controlled with these epitaxial film series deposited with variable PLD oxygen partial pressure. A nearly linear dependence of resistivity on carrier concentration was found. In the deposition chamber with the smaller 50 mm distance from PLD target to the substrate, we found a strong dependence of carrier concentration on oxygen partial pressure adjusted from $5\times10^{-4}$ up to 0.04 mbar (see [56]). The Hall mobility at room temperature of nominally undoped ZnO films on *c*-plane sapphire grown by a multistep PLD process with low-temperature nucleation layers [51] is shown in Fig. 7.15. The highest mobility values are obtained only in a narrow carrier concentration range of $(2\text{–}5)\times10^{16}\,\mathrm{cm}^{-3}$. A much weaker dependence of carrier concentration and Hall mobility on the oxygen partial pressure was found for PLD growth at 100 mm target to substrate distance.

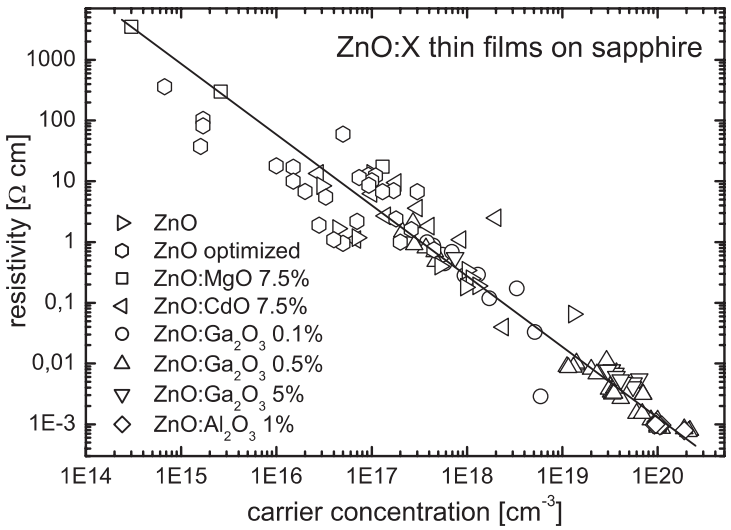


**Fig. 7.14.** Resistivity vs. carrier concentration at 300 K of undoped and doped PLD ZnO thin films on sapphire [56]. The legend gives the maximum concentrations of the dopant oxides in the ZnO targets in weight-%. The optimized ZnO films show lower intrinsic n-type conductivity. For each dopant element, series of films grown at different PLD oxygen pressures are included

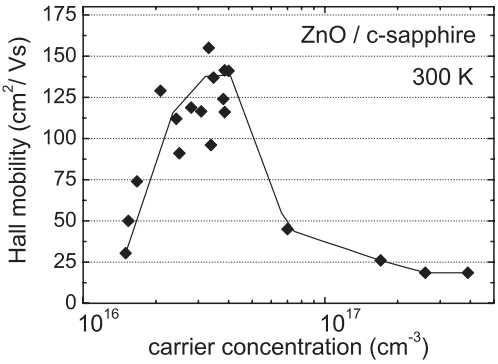


**Fig. 7.15.** Peak behavior of Hall mobility at 300 K of undoped ZnO thin films on *c*-plane sapphire at carrier concentrations around $3 \times 10^{16}\,\mathrm{cm}^{-3}$. For these particular growth conditions with a target-to-substrate distance of 50 mm, a low-temperature nucleation layer was used. Reprinted with permission from [51]

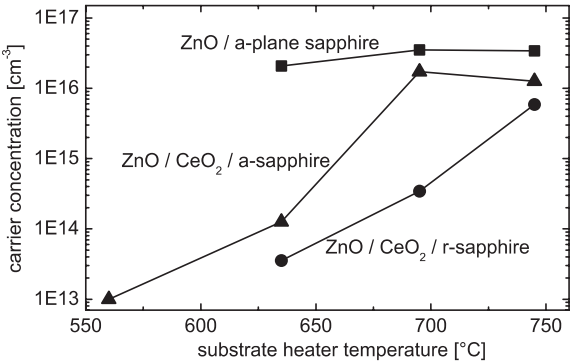


**Fig. 7.16.** Growth temperature-dependent reduction of carrier concentration (300 K) of ZnO films on sapphire due to introduction of $CeO_2$ buffer layers. The growth temperature is about 50°C lower as the given heater temperature. Hall measurements by H. von Wenckstern

For that, high Hall mobility values well above 100 up to $150\,\mathrm{cm}^2\,(\mathrm{V\,s})^{-1}$ were obtained reproducibly for carrier concentrations from about $6 \times 10^{15}$ up to $3 \times 10^{16}\,\mathrm{cm}^{-3}$.

Buffer layers deposited on the sapphire substrates prior to ZnO deposition reduce the Al diffusion and thereby the n-type carrier concentration, as shown in Fig. 7.16. The use of $CeO_2$ buffer layers is well established from the deposition of high-$T_c$ superconducting thin films on sapphire [7, 8, 10]. However, the effect of the $CeO_2$ buffer layer decreases with increasing growth temperature due to the limited thermal stability of the 10 nm thin layer as shown in Fig. 7.16. To give a clear evidence for the reduced interdiffusion, Fig. 7.17 shows the isotope intensity depth profiles of ZnO films grown

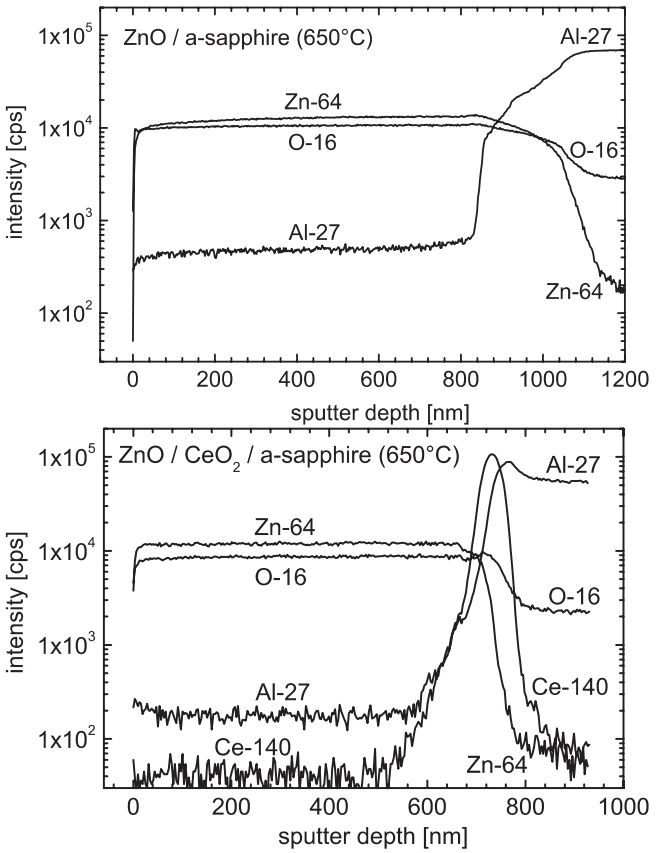


**Fig. 7.17.** SNMS isotope intensity sputter depth profiles of ZnO films grown at 650°C without (*top*) and with (*bottom*) $CeO_2$ buffer layer. The buffer layer with a thickness of about 50 nm reduces the interdiffusion of Al and Zn into ZnO and sapphire, respectively, and thereby the concentration of n-type carriers in the ZnO film

without and with $CeO_2$ buffer layer. The reduction of the Al and Zn concentrations within the ZnO film and the $Al_2O_3$ substrate, respectively, is obvious. Instead of $CeO_2$, MgO buffer layers show slightly improved barrier properties, so that mainly MgO buffer layers are used [57] to grow semi-insulating ZnO films for conversion experiments into the p-type conducting state by acceptor doping [58].

A deeper insight into the lateral electrical homogeneity of the films, the limiting mechanisms of the Hall mobility, and the thermal activation energies of shallow and deep defect levels can be gained by temperature-dependent Hall and deep level transient spectroscopy (DLTS) measurements [57,59,60]. To give an example, the temperature dependence of the Hall mobility and

of the carrier concentration of a series of optimized ZnO films grown at different oxygen partial pressures is shown in Fig. 7.18. The ZnO film thickness is around 1 µm. The temperature dependence of the mobility is similar for the films grown at oxygen partial pressures from $3 \times 10^{-3}$ to $3 \times 10^{-2}$ mbar, whereas the film grown at higher pressure of $10^{-1}$ mbar shows a lower mobility over the whole temperature range, a shifted maximum, and a decreasing temperature dependence for low temperatures. The corresponding carrier concentration in dependence on the inverse temperature is shown in Fig. 7.18. The three films grown at lower PLD oxygen pressure show semiconductor-like decrease in carrier concentration with decrease in temperature. The cutoff of the carrier concentrations with decrease in temperature is due to the detection limit of the Hall voltage in the $10^{14}$ cm$^{-3}$ range. Therefore, the mobility

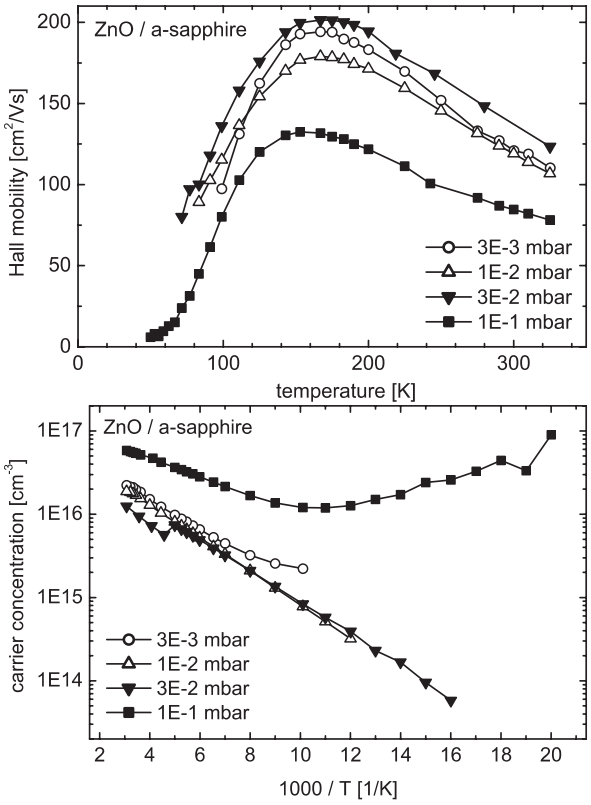


**Fig. 7.18.** Temperature dependence of the Hall mobility (*top*) and of the carrier concentration (*bottom*) of undoped PLD ZnO thin films on *a*-plane sapphire grown at different oxygen partial pressures (see *legends*). Note the different temperature scales. The film grown at highest pressure shows an unusual metal-like temperature dependence of the carrier concentration for $T < 90$ K. By H. von Wenckstern [59]

**Table 7.5.** Energetic positions below the conduction band edge ($E_c$) and densities of shallow ($H_i$, $Al_{Zn}$) and deep (E1–E5) donor-like defect levels (traps) in ZnO identified by temperature-dependent Hall effect and deep level transient spectroscopy, respectively, in undoped PLD films and single crystals grown by seeded chemical vapor deposition (Eagle Picher), taken from H. von Wenckstern [57]

| | PLD thin film | | Single crystal | |
|---|---|---|---|---|
| Defect | $E_c - E_t$ (meV) | $N_t$ ($cm^{-3}$) | $E_c - E_t$ (meV) | $N_t$ ($cm^{-3}$) |
| $H_i$ | | | $37 \pm 2$ | $(1.3 \pm 0.2) \times 10^{17}$ |
| $Al_{Zn}$ | $65 \pm 2$ | $(6.0 \pm 1.0) \times 10^{16}$ | | |
| E1 | $110 \pm 20$ | $(1.4 \pm 0.2) \times 10^{15}$ | $100 \pm 20$ | $(1.4 \pm 0.2) \times 10^{15}$ |
| E3 | $290 \pm 30$ | $(6.2 \pm 0.7) \times 10^{15}$ | $300 \pm 30$ | $(2.2 \pm 0.4) \times 10^{14}$ |
| E4 | | | $540 \pm 40$ | $(1.8 \pm 0.4) \times 10^{14}$ |
| E5 | | | $840 \pm 50$ | $(4.4 \pm 0.5) \times 10^{14}$ |

and carrier concentrations can be given for $T < 100\,K$ for these films only. In difference, the film grown at 0.1 mbar could be measured down to about 50 K. The carrier concentration decreases down to about 100 K and than shows a metal-like increasing behavior at lower temperature. The origin of this behavior is not completely clear up to now. The Hall data could be modeled with the assumption of a very thin, highly n-type conductive degenerate layer near to the interface of the substrate [59]. By fitting the temperature-dependent mobility data of PLD ZnO films, the grain boundary scattering of the carriers was identified as the limiting mechanism in PLD ZnO thin films on sapphire, thus opening potential for further film optimization [61].

In addition to temperature-dependent Hall measurements, deep level transient spectroscopy (DLTS) was performed using high-quality Schottky contacts [60] (see also Sect. 7.5.3 with Fig. 7.31) to obtain thermal activation energies and densities of the electrically active defects in PLD ZnO thin films and ZnO single crystals. To summarize these results, the obtained energetic positions and the densities of shallow and deep donor-like defect levels in a PLD ZnO thin film and a ZnO single crystal from Eagle Picher are given in Table 7.5 [57, 61]. The shallow defect levels in ZnO can be assigned to the donors $H_i$ at interstitial position and $Al_{Zn}$ at Zn-position (compare [62]). However, the chemical identity of the deep donor levels is still under discussion; therefore, they are usually assigned as E1 to E5.

### 7.4.4 Luminescence of PLD ZnO Thin Films on Sapphire

Photo- and cathodoluminescence (PL, CL) measurements at liquid helium temperature are sensitive tools for investigation of the optical recombination properties [62] of the PLD ZnO films. In ZnO, the information depth of PL using a 325 nm He–Cd laser is only about 60 nm [63], corresponding to

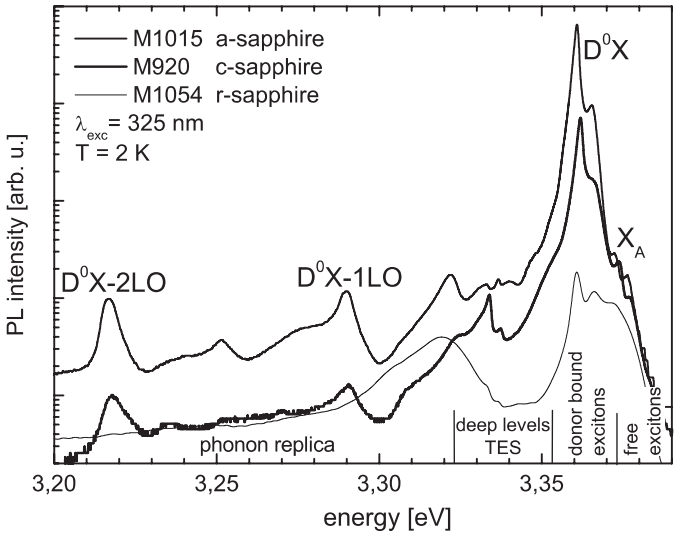


**Fig. 7.19.** Photoluminescence spectra (2 K) of PLD ZnO thin films on *a*-plane, *c*-plane, and *r*-plane sapphire substrates [63]. All films were grown at about 650°C and at $1.6 \times 10^{-2}$ mbar oxygen pressure. The FWHM of the most intense donor bound exciton peaks $D^0X$ of the ZnO films are 1.4 meV on *a*-plane sapphire, 1.7 meV on *c*-plane sapphire, and 2.6 meV on *r*-plane sapphire. The spectral resolution of the PL setup was 1 meV at 3.35 eV

the topmost surface layer even in PLD thin films. CL has higher information depth, being about 250 nm for 5 keV acceleration voltage of the electron beam, and about 750 nm for 10 keV electron energy [54]. The diameter of the laser beam in PL, i.e., the lateral resolution, is usually a few 100 µm, whereas the electron beam in CL can be focused down to about 20 nm diameter at the surface, thus allowing, for example, CL line scans on cross-sections of micrometer thin films, and CL intensity and CL wavelength scans at the $10 \times 10\,\mu m^2$ area range.

Figure 7.19 shows PL spectra recorded at 2 K for 2.2, 0.7, and 1.5 µm thick PLD ZnO films on *a*-plane, *c*-plane, and *r*-plane sapphire, respectively [63]. The full widths at half maximum (FWHM) of the most intense bound exciton peaks are 1.4, 1.7, and 2.6 meV for *a*-, *c*-, and *r*-sapphire, respectively. The film on *a*-plane sapphire shows the narrowest FWHM among the films under investigation and the free A-exciton ($X_A$) is most clearly resolved, thus indicating best structural properties of ZnO on *a*-plane sapphire. The ZnO films on *a*- and *c*-plane sapphire grow *c*-axis textured, whereas films on *r*-plane sapphire grow *a*-axis oriented with the ZnO *c*-axis being in-plane, as demonstrated already in Fig. 7.4. The PL spectrum of the film on *r*-plane sapphire shows no phonon replica, probably due to the changed ZnO orientation.

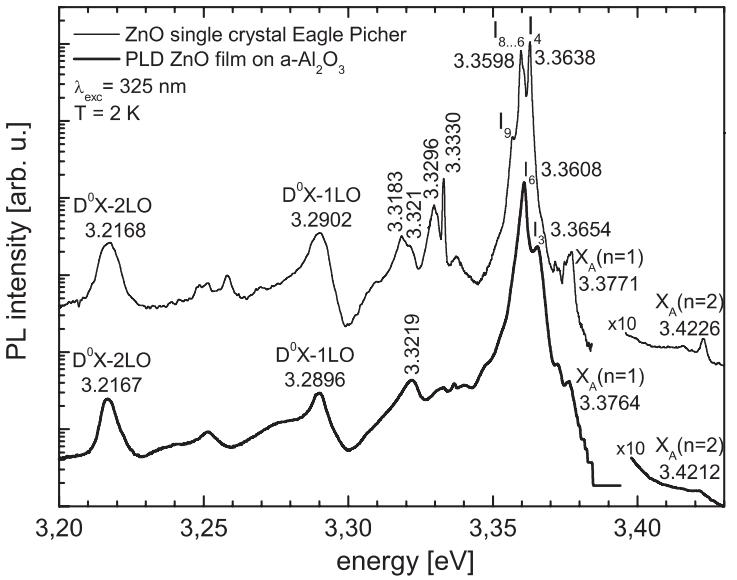


**Fig. 7.20.** Comparison of PL spectra at 2 K of a 2.2 $\mu$m thick ZnO film on *a*-plane sapphire and of a ZnO bulk single crystal grown by seeded chemical vapor deposition (Eagle Picher), both (0001) oriented. The PLD film was deposited by a 4-step PLD process [51] and shows a PL spectrum very similar to that of the single crystal. The energies of the assigned luminescence peaks are given in [eV]. The spectral resolution of the PL setup is 1 meV at 3.35 eV [63]

Figure 7.20 compares the PL spectra of the ZnO film on *a*-plane sapphire with that of a ZnO bulk single crystal from Eagle Picher. General features, as the most intense lines of free and bound excitons, and the phonon replica , appear in both spectra and demonstrate the single crystalline-like structural quality of optimized PLD ZnO thin films in the near-surface region. The most intense donor bound exciton peak of the ZnO films on sapphire (Fig. 7.20) is the $I_6$ peak, which can be attributed according to [62,64] to the Al donor. The FWHM of the donor bound exciton peaks $I_{8..6}$ and $I_4$ of the single crystal are less than 1 meV, compared to 1.4 meV for $I_6$ of the film. From the excitonic PL peak energies $X_A$ $(n = 1)$, $X_A$ $(n = 2)$ and the first and second phonon replica of $D^0X$ shown in Fig. 7.20, the band gap energies, the exciton binding energies, and the LO-phonon energies were calculated using the effective mass model at $k = 0$ [63]. Table 7.6 summarizes these results for the ZnO single crystal and the PLD thin film on *a*-plane sapphire. Within the error limits, the values for the single crystal, the PLD thin film, and published values [62] are in good agreement, thus proving again the single crystal-like structural and optical properties of the near-surface region of the PLD thin films.

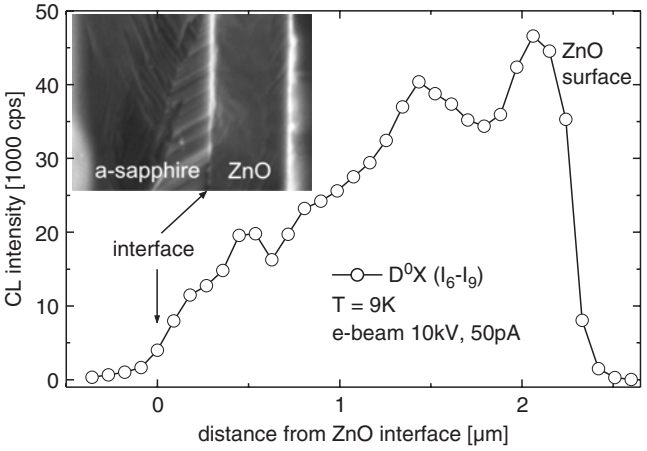


**Fig. 7.21.** CL line scan at 9 K of the intensity of the bound exciton transitions $I_6$ to $I_9$ measured at the cross-section of a 2.2 µm thick ZnO film on *a*-plane sapphire from the sapphire substrate to the ZnO film surface. The inset shows the corresponding SEM image of the cross section. Measured by J. Lenzner

**Table 7.6.** Comparison of band gap energies $E_g$, exciton binding energies $E_{XB}$, and 1LO and 2LO phonon energies $\hbar\omega_{1LO}$ and $\hbar\omega_{2LO}$, calculated from the PL peak energies of a ZnO single crystal (Eagle Picher) and a PLD ZnO thin film on *a*-plane sapphire at 2 K, as given in Fig. 7.20 [63]

| | $E_g$ (eV) | $E_{XB}$ (meV) | $\hbar\omega_{1LO}$ (meV) | $\hbar\omega_{2LO}$ (meV) |
|---|---|---|---|---|
| Single crystal Eagle Picher | $3.4381 \pm 0.0015$ | $61 \pm 1$ | $72.6 \pm 1$ | $73.4 \pm 1$ |
| PLD ZnO film on a-sapphire | $3.4364 \pm 0.0015$ | $60 \pm 1$ | $71.2 \pm 1$ | $72.9 \pm 1$ |

Thinner ZnO films on sapphire, i.e., with thickness $\leq 0.5$ µm, show often less intense PL spectra with broader excitonic peaks, which are due to the increasing density of dislocation lines near the interface, as shown in the TEM cross-section Fig. 7.6. To further investigate this phenomenon, a cross-section of a ZnO film was prepared by simply breaking a 2.2 µm thick film with the substrate and measuring a CL line scan of the excitonic peak intensity from the interface sapphire/ZnO as start point up to the surface of the ZnO film, as shown in Fig. 7.21 together with the SEM view on the cross-section. The CL intensity increases from nearly zero at the sapphire/ZnO interface up to the maximum near the surface of the ZnO film, thus supporting again the correlation of low defect density and high luminescence intensity. In summary, near the surface of PLD ZnO thin films on *a*- and *c*-plane sapphire, structural quality and optical luminescence properties are very similar to those of ZnO bulk single crystals.

### 7.4.5 Chemical Composition of Doped PLD ZnO Films and Doping Effects

The flexible doping and alloying of ZnO thin films is probably the most prominent advantage of PLD in comparison to other deposition techniques. Therefore, a variety of dopants has been investigated in PLD ZnO films, as will be shown in the following. The addition of the dopant is done by mixing the dopant element in form of the appropriate oxide into the ZnO powder used for target preparation. By ball milling the powder mixture, a homogenous distribution of the dopant will be achieved. After pressing the powder, the target will be sintered at 900–1,150°C in air for 12 h. Concerning the chemical composition of the thin films grown from the multielement targets in the PLD process, usually a reproduction of the target composition in the thin film is expected, as explained already in Sect. 7.1. However, depending on the properties of the deposited atomic species and the substrate temperature, this rule is not generally valid for all materials.

Unfortunately, many of the doped and alloyed ZnO thin films important for future optoelectronic applications show deviations of their chemical composition compared to that of the PLD target. The most pronounced examples ZnO:Li, MgZnO, and CdZnO of composition deviations are demonstrated in dependence on the oxygen partial pressure in Figs. 7.22 and 7.23 in contrast to ZnO:Mn, which shows a nearly 1:1 transfer. Averaged over the oxygen partial pressure, the dopant composition, and other deposition parameters, Table 7.7 summarizes the average composition transfer factors from the PLD target into the grown film and calls the dopant oxide used for target preparation. The film compositions were analyzed by ion beam analysis using combined Rutherford backscattering spectrometry (RBS) and particle induced X-ray emission (PIXE) with 1.2 MeV $He^+$ and $H^+$ ions, respectively [65]. For most dopant elements a transfer factor above 1 was determined (Table 7.7). That means that the chemical composition of the dopant element in relation to Zn is increased by the PLD process. However, some dopant elements, as P, Ni, and Cu, and Cd show transfer factors considerably below 1. To understand this different behavior of the dopant elements in the PLD process (for the PLD parameters see Table 7.3), in Table 7.7 the evaporation temperature of Zn and of the dopant elements at normal conditions is given. The element with the lower evaporation temperature may evaporate preferably from the heated substrate, thus yielding a lower composition of this particular element in the film. For example, P and Cd show lower evaporation temperatures as Zn, thus explaining the low transfer factors of these elements into the ZnO-based films. In the case of Cd, in addition a low solubility of CdO in ZnO of a few at. % is reported (see [56, 72]), thus explaining the extremely low transfer factor of Cd. However, the correlation of low transfer factor and low evaporation temperature does not apply for Ni and Cu as neighbor elements to Zn in the periodic system. In contrast, Mg has the highest transfer factor of all dopant elements. Probably, the preferential ablation of ZnO out of the

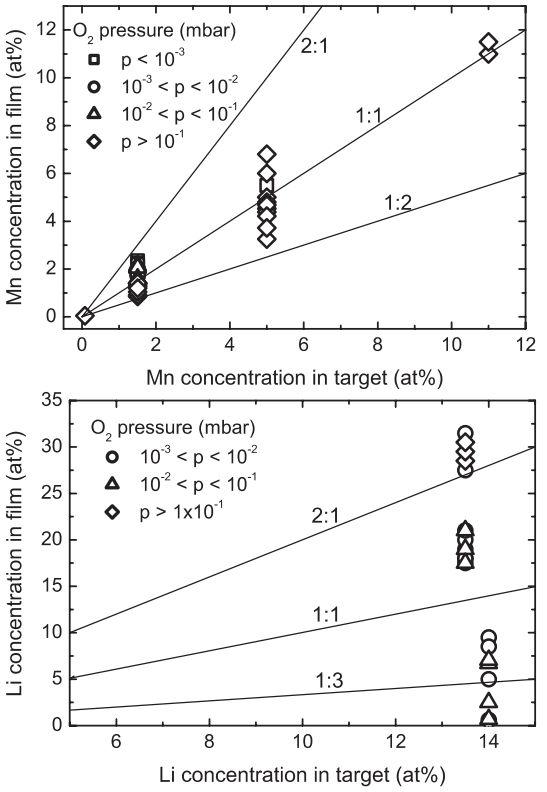


**Fig. 7.22.** Transfer of the chemical composition of Mn (*top*) and Li (*bottom*) from the PLD ZnO:Mn and ZnO:Li targets, respectively, into the thin films, for different target compositions and PLD gas pressures [65]. Further variation of concentrations is due to different growth temperature and other PLD parameters. Li shows the largest scattering among all investigated dopant elements (see Table 7.7 and Fig. 7.23) due to the properties of the small Li atoms. Reprinted with permission from [65]

MgZnO target is an additional reason for the Mg-enriched films because of the low optical absorption coefficient of MgO with $E_g$ around 8 eV for the excimer laser light at 248 nm wavelength. The observed continuous shift of the MgZnO film composition with the ablation state of the MgZnO target supports this assumption of the preferential target ablation.

Because the current research efforts on the II–VI semiconductor ZnO are directed for example to blue and UV-optoelectronic devices, the cleanness requirements of the established semiconductor processes should be applied also for ZnO, if possible. To get a first estimate about the trace element contamination of the PLD ZnO films, we analyzed two undoped ZnO thin films by PIXE/RBS for their trace element concentration [65] as given in Table 7.8. For most elements listed in Table 7.8, the detected trace element

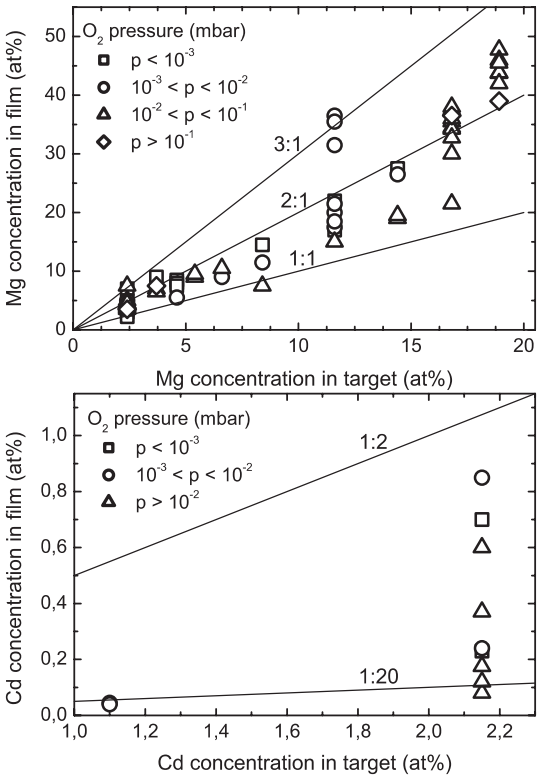


**Fig. 7.23.** Transfer of the chemical composition of Mg (*top*) and Cd (*bottom*) from the PLD MgZnO and CdZnO targets, respectively, into the thin films, for different compositions and PLD gas pressures [65]. Further variation of concentrations is due to different growth temperature and other PLD parameters. Reprinted with permission from [65]

concentrations are near the detection limits of the ion beam analysis, which is around 10 ppm. At the edges of the 32.8 mm diameter wafers remarkable concentrations of the elements K, Ca, Ti, Cr, and especially Fe were found. Most of these elements are constituents of stainless steel and the stainless steel substrate holder and the hot parts of the substrate heater in the PLD chamber are most probably the source of the Fe and Cr contamination of the film edges. In the center of both investigated films, the impurity concentrations of nearly all elements are near the detection limit of the ion beam analysis, thus demonstrating the high potential of PLD to deposit contamination free films.

To provide an extended overview on the various PLD-based activities of the Leipzig Semiconductor Physics Group, Table 7.9 summarizes the published investigations on ZnO-based thin films. The dopants were arranged in four groups, namely (1) the n-type donors Al and Ga, (2) the potential

**Table 7.7.** Transfer factor of dopant composition (in ZnO matrix) from the PLD target into the deposited thin film as determined by RBS/PIXE by D. Spemann [65], averaged over the dopant composition and the oxygen partial pressure, compare also Figs. 7.22 and 7.23

| dopant element $x$ to ZnO | Oxide of Dopant element in target | Evaporation temperature of the dopant element (°C) | Transfer factor of dopant composition from PLD target into the film $c_x$(film)/$c_x$(target) |
|---|---|---|---|
| Undoped | Matrix:ZnO | 907 (Zn) | 1.0 (Zn) |
| Li | $Li_3N$ | 1,342 | $1.37 \pm 0.72$ |
| Mg | MgO | 1,090 | $1.86 \pm 0.49$ |
| Al | $Al_2O_3$ | 2,519 | $1.56 \pm 0.44$ |
| P | $P_2O_5$ | 280 | $0.50 \pm 0.01$ |
| Ti | $TiO_2$ | 3,287 | $1.15 \pm 0.43$ |
| Mn | $MnO_2$, MnO | 2,061 | $1.03 \pm 0.28$ |
| Fe | $Fe_2O_3$, FeO | 2,861 | $1.47 \pm 0.16$ |
| Co | CoO | 2,927 | $1.23 \pm 0.09$ |
| Ni | NiO | 2,913 | $0.15 \pm 0.02$ |
| Cu | CuO, $Cu_2O$ | 2,562 | $0.74 \pm 0.25$ |
| Ga | $Ga_2O_3$ | 2,204 | $1.54 \pm 1.04$ |
| Cd | CdO | 767 | $0.09 \pm 0.12$ |
| Sb | $Sb_2O_3$ | 1,587 | $1.71 \pm 0.32$ |

The dopant oxide is used for target preparation and the evaporation temperatures of the dopant elements partially explain the deviations of the transfer factor from 1.0

**Table 7.8.** Typical atomic concentrations of trace elements (all values given in ppm) in large-area diameter ZnO thin films on sapphire grown in a stainless steel PLD chamber with stainless steel substrate holder and KANTHAL-wire in $Al_2O_3$ ceramic tubes as heater element at about 650°C

| Sample | Si | K | Ca | Ti | V | Cr | Mn | Fe | Ni | Cu |
|---|---|---|---|---|---|---|---|---|---|---|
| E391c | 1,342 | <16 | 24 | <11 | <14 | <15 | 20 | 35 | <67 | <153 |
| E391e | <901 | 30 | 28 | <13 | <16 | 28 | <19 | 1,069 | <69 | <166 |
| E392c | <971 | <30 | <24 | <21 | <24 | 50 | <26 | <33 | <104 | <215 |
| E392e | <1,272 | 54 | 51 | 27 | <29 | 85 | 41 | 206 | <103 | <243 |
| DL | 901 | 16 | 12 | 11 | 14 | 15 | 17 | 20 | 67 | 153 |

The PLD target was sintered from 99.9995 at. % ZnO powder. DL is the minimum detection limit of the combined PIXE/RBS analysis with 1.2 MeV protons. Each wafer (32.8 mm diameter) was analyzed at center (c) and edge (e) position. Measured by D. Spemann

p-type acceptors N, Li, P, and Sb, (3) the isoelectronic alloys ZnO:MgO and ZnO:CdO for tuning the electronic bandgap, and finally (4) the 3d-elements Sc, Ti, Mn, Fe, Co, Ni, Cu to obtain diluted magnetic semiconductors (DMS) with both ferromagnetic and semiconducting properties to employ the spin state for information transfer or storage in innovative spinelectronic devices.

**Table 7.9.** Overview about published research results of the Leipzig Semiconductor Physics Group on ZnO-based PLD thin films

| Dopant | Investigated effect of doping | Refs. |
|---|---|---|
| Al, Ga | n-type carrier concentration in dependence on PLD oxygen partial pressure | [56] |
| Al | Al-doped ZnO thin film as ohmic back contact of ZnO films with Pd Schottky contact on top, improved frequency response enables capacitance spectroscopy DLTS | [57, 59] |
| Mg | Infrared dielectric functions and phonon modes of wurtzite MgZnO, and Mg-rich cubic MgZnO films by spectroscopic IR ellipsometry 380–1,200 $cm^{-1}$, 360–1,500 $cm^{-1}$, respectively. (See also Sects. 3.3 and 3.4.3) | [66–68] |
| Mg | Dielectric functions, refractive indices, and band gap energies of wurtzite MgZnO, and Mg-rich rocksalt MgZnO films by UV–vis ellipsometry 1–5 eV (See also Sects. 3.6.2 and 3.7.2) | [69–71] |
| Mg | Quantum confinement PL of MgZnO/ZnO hetero- and double-heterostructures grown by PLD | [53] |
| Mg, Cd | blueshift, redshift of optical absorption edge in dependence on Mg, Cd content | [56] |
| Cd | Incorporation of Cd by MOCVD (max. 8 at. %), XRD, PL in dependence of Cd content, comparison with Cd incorporation in sequential PLD of ZnO/CdO multilayers | [72, 73] |
| Fe, Sb, Al, Ga, Li | Phonon modes by Raman spectroscopy, comparison with published modes in ZnO:N (See also Sect. 3.4.2) | [74] |
| Li, N | Attempts for p-type conducting ZnO films, photoluminescence | [75] |
| N, P, Sb | Electrical activity of group V acceptors in ZnO | [76] |
| P | Strong indication for p-type conducting surface areas on P-doped ZnO thin films by scanning capacitance microscopy SCM | [58] |
| Mn | Magnetic hysteresis (SQUID), magnetic domains (MFM), luminescence (PL), PLD parameters of ferromagnetic ZnO:Mn films, | [77, 78] |
| Mn | EPR of ZnO:Mn films, valence state, hyperfine structure, fine structure parameter | [79, 80] |
| Co, Mn, Ti | Thermal activation energy and density of deep donor-like levels in 3d-doped ZnO films, Schottky contacts (DLTS) | [81, 82] |
| Ti, Co, Mn | Magnetoresistance in dependence of dopant composition from 0.02 up to 2 at. %, temperature and magnetic field up to 6 T, for ZnO:Ti magnetic domains (MFM) | [78, 83] |
| Co, Al | Magnetoresistance in dependence of film thickness, temperature, and magnetic field up to 6 T | [84] |
| Gd, Nd | Deep levels by DLTS, magnetoresistance, anomalous Hall effect, magnetic domains for ZnO:0.1 at. % Nd by MFM | [85] |

**Table 7.9.** (continued)

| Dopant | Investigated effect of doping | Refs. |
|---|---|---|
| ZnO/ $BaTiO_3$/ ZnO | Electro-optical effects of BTO, ZnO/BTO, and ZnO/BTO/ZnO heterostructures with fixed/switchable polarization, IV and CV, ferroelectric hysteresis | [86–88] |

The results are arranged according to the aim of doping or alloying, namely (1) n-type conductivity, (2) bandgap-tuning and quantum confinement, (3) potential p-type conductivity, and (4) ferromagnetic behavior. In addition, (5) ZnO/$BaTiO_3$ heterostructures as combination of ZnO with fixed and $BaTiO_3$ with electrically switchable polarization are included

Additionally, (5) ZnO/$BaTiO_3$ heterostructures as combination of ZnO with fixed polarization and $BaTiO_3$ with electrically switchable polarization are included in Table 7.9. Highlights of the Leipzig research on doped and alloyed PLD ZnO films include the measurement of the dielectric function of MgZnO films over the whole mixing range from pure ZnO to pure MgO in the optical IR and in the vis–UV spectral range using spectroscopic ellipsometry, the observation of quantum confinement effects in MgZnO/ZnO/MgZnO heterostructures [53], and the successful observation of p-type conducting surface areas in P-doped ZnO films grown by PLD [58]. With respect to ferromagnetism in ZnO films doped with various 3d- and 4f-elements, the flexibility and the high potential of PLD is demonstrated in Fig. 7.24, where stripe-like or bubble-like magnetic domains on the surface of Mn-, Co+Al-, and Ti-, and Nd-doped ZnO thin films were imaged by magnetic force microscopy (MFM). As a direct proof of the magnetic effect, the corresponding atomic force microscopy (AFM) image of the same surface area of each particular film is given in Fig. 7.24. Finally, the investigation of shallow and deep defect levels in Mn-, Co-, and Ti-doped ZnO thin films [77, 81, 83] should be mentioned, which became possible by the introduction of an advanced Schottky contact configuration for the doped PLD ZnO thin films using a degenerately doped ZnO:Al film as ohmic back contact [57, 59]. As a reference, Table 7.5 in Sect. 7.4.3 compares the shallow and deep defect levels in undoped ZnO films and a ZnO single crystal as determined by temperature-dependent Hall effect and DLTS. Only the innovative front-to-back Schottky contact configuration provides low series resistance and therefore improved frequency response up to 10 MHz, which allows for the first time DLTS measurements of deep level activation energies of undoped and variously doped PLD ZnO thin films.

## 7.5 Demonstrator Devices with PLD ZnO Thin Films

In this section, some selected recent application-oriented results of PLD ZnO films and heterostructures will be presented in more detail. In particular, (a) large-area ZnO films on sapphire optimized for high cathodoluminescence

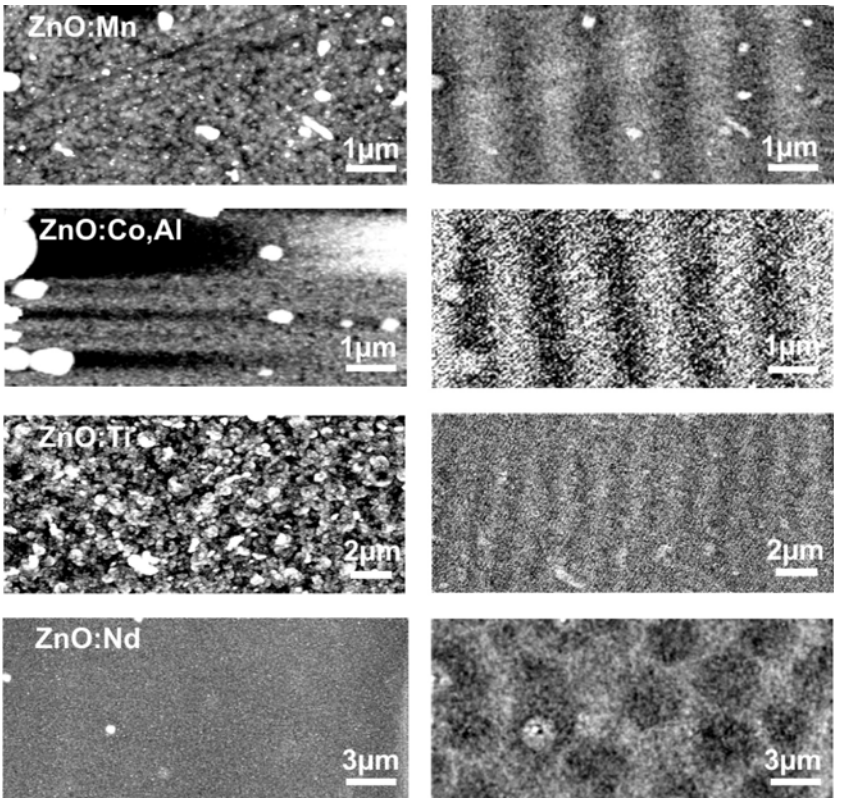


**Fig. 7.24.** AFM (*left*) and MFM (*right*) images of identical positions of 3d- or 4f-element doped PLD ZnO films on sapphire (from top): ZnO:Mn(2.56 at. %) [77], ZnO:Co(0.2 at. %)Al(0.5 at. %) [84], and ZnO:Ti(9.9 at. %) [78] (see also [83]), and ZnO:Nd(0.1 at. %) [85]. The MFM images taken with a lift scan height of 50 nm of the low-coercivity tip clearly demonstrate the stripe-like or bubble-like magnetic domain formation. The z-scales of the AFM/MFM images are 50 nm/0.8° for ZnO:Mn, 50 nm/0.2° for ZnO:Co,Al, 100 nm/0.5° for ZnO:Ti, and 10 nm/0.8° for ZnO:Nd, respectively. Measured by H. Schmidt and M. Ungureanu

yield for scintillator applications, (b) Bragg mirrors consisting of oxide multilayers with maximum reflectivity at 3.3 eV together with quantum confinement effects in MgZnO/ZnO/MgZnO quantum well structures, and (c) Pd Schottky diodes to PLD ZnO thin films with optimized rectifying behavior are reported. The quantum well structures and the Schottky contacts were already mentioned in Sect. 7.4.5. Finally, an overview on international highlights of PLD ZnO thin films and heterostructures, e.g., the first blue ZnO-based LED, will be given.

### 7.5.1 Large-area ZnO Scintillator Films

We patent-pended a pulsed laser deposition (PLD) process [89,90] for n-type conducting ZnO thin films, which show high CL intensities under optimized growth conditions. ZnO is described as a new scintillator material class because of its high luminescence intensity and the short decay time in the nanosecond range [91, 92]. Because of increased data rate and resolution in state of the art electron microscopic imaging there is a need for more homogeneous, faster, and if possible brighter scintillators based on epitaxial ZnO thin films to replace the polycrystalline ZnO-based phosphors.

We investigated ZnO thin films grown from nominally undoped ZnO targets in either reducing or oxidizing environments, namely in $N_2$, $N_2O$, and $O_2$ background gases, and in a wide 5 orders of magnitude range of background gas pressure from $3 \times 10^{-4}$ to 10 mbar, as shown in Fig. 7.25 [89]. Because the luminescence spectra have to be detected both from the film side (in reflection) and through the sapphire substrate (in transmission) [90], the films were grown on double-side epi-polished *a*-plane sapphire substrates of the size $10 \times 10\,mm^2$ and 32.8 mm diameter. For the PLD growth of ZnO films with area larger than $1\,cm^2$ we employ the so called offset-PLD with parallel target and substrate arrangement and a target to substrate distance of 100 mm [10]. Films grown at about 1 mbar background pressure show the highest normalized excitonic CL intensity, independently of the kind of gas, as shown in Fig. 7.25. This maximum of the near-band-edge luminescence in undoped ZnO films is clearly correlated with maxima of both the free carrier concentration and the Hall mobility. For the high growth pressure around 1 mbar, the average surface roughness of the films is considerably increased, as shown in Fig. 7.25. However, a rough surface probably promotes the outcoupling of the generated light from the ZnO film into the environment.

Figure 7.26 shows typical room-temperature CL spectra of three ZnO thin films deposited at the optimum pressure of 0.9 mbar for the three background gases. All spectra show the dominating excitonic near-band-edge luminescence peak with a maximum at around 3.25 eV and the two-to-three orders of magnitude weaker defect-dominated luminescence band in the visible spectral range. The intensity of the defect-dominated CL signal increases in the order of used $N_2$ – $N_2O$ – $O_2$ gas. To explain CL spectra taken in dependence on the excitation voltage and for detection of the luminescence light on the film or the substrate side of the film sample, a model based on self absorption of the generated photons in the ZnO film was developed [90,93]. This model was also used to explain the origin of the remarkable splitting and broadening of the excitonic CL peak of films grown in oxygen (see Fig. 7.26).

Both small crystallites with size in the 300 nm range and huge single crystalline regions with hexagonal shape in the 20 µm size range are able to emit maximum CL intensity, as shown in Fig. 7.27 [90]. These substantial differences of the surface morphology are due to the growth conditions, including substrate properties. However, up to now they cannot be related directly to

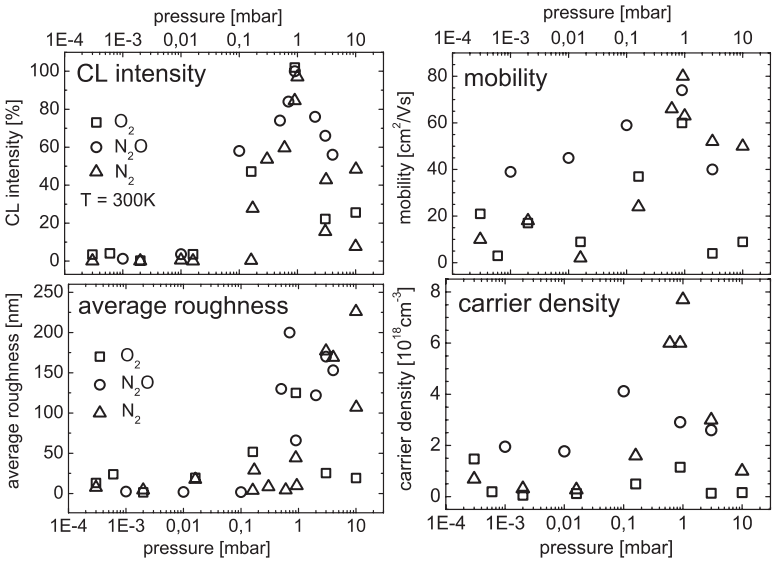


**Fig. 7.25.** CL intensity, Hall mobility, and carrier concentration at 300 K of PLD ZnO thin films on a-plane sapphire show maxima around 1 mbar background gas pressure of $O_2$, $N_2O$, and $N_2$ during growth at 100 mm target substrate distance, indicating the growth condition for ZnO thin film scintillators [89]. The average surface roughness is considerably increased at the high growth pressure of 1 mbar

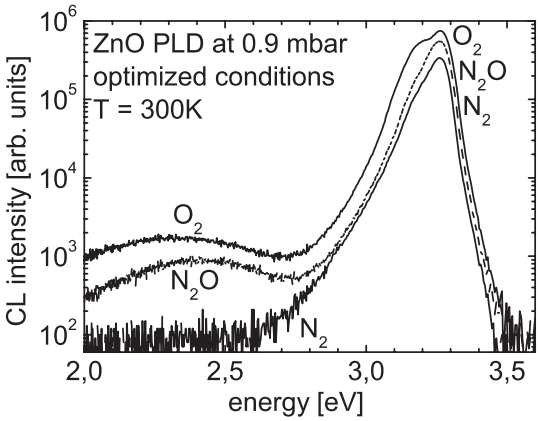


**Fig. 7.26.** Typical room temperature CL spectra of ZnO thin films grown at optimized $O_2$, $N_2O$, and $N_2$ background gas pressure of 0.9 mbar [89]. The film grown in $O_2$ shows splitting and broadening of the excitonic peak. Only the film grown in $N_2$ shows nearly no green luminescence around 2.3 eV photon energy

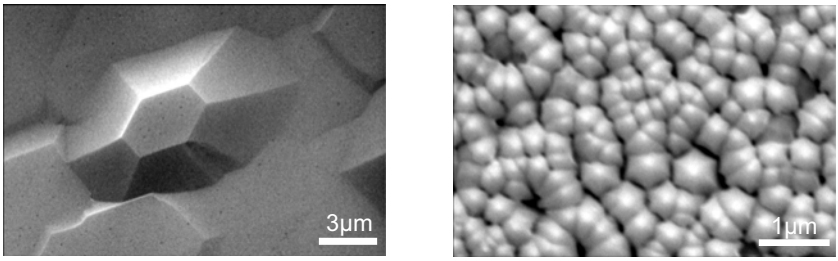


**Fig. 7.27.** SEM images of ZnO thin films on *a*-plane sapphire grown in 1 mbar oxygen. Both films show very high UV CL intensity, but very different film morphology due to different growth conditions [90]

adjustable PLD parameters. Probably, variations of the miscut of the *a*-plane sapphire substrates which is specified within a range of $\pm 1^\circ$ could be the origin for the different film morphologies.

### 7.5.2 Bragg Reflector Mirrors and ZnO Quantum Well Structures

Dielectric Bragg reflector mirrors made from thin film heterostructures are used for example to enhance the optical confinement in resonators of semiconductor lasers. For the future application of ZnO as the active laser medium at room temperature, Bragg reflectors for the excitonic emission energy of ZnO, i.e., for 3.3 eV, are needed. To grow oxide based Bragg mirrors with a high reflectivity near 100%, the PLD technique had to be qualified concerning a precise control of the single layer thicknesses, the chemical composition, and so the refractive indices. We found that MgZnO could not be used as one of the layer materials because of the reasons mentioned in Sect. 7.4.5. We failed to obtain a stable MgZnO composition of consecutively deposited layers. Therefore, first attempts of a 9.5 pair ZnO-MgO Bragg structure on sapphire showed a reflectivity of 85% at 2.3 eV phonon energy [94]. The isotope intensity depth profile of this particular Bragg mirror is shown in Fig. 7.28. The thickness and the complex dielectric functions of the Bragg mirrors were derived from spectroscopic ellipsometry by fitting the measured data with an appropriate layer model [95, 96]. The refractive index data were obtained from single layers of the used oxide materials.

Further improvement of the structural and optical properties of the PLD Bragg mirrors was achieved by substituting ZnO by yttria stabilized zirconia (YSZ, with typically 9 at. % $Y_2O_3$), as demonstrated in Fig. 7.29. A considerable increase of the maximum reflectivity of the Bragg structures from about 90–99% was realized by doubling the number of YSZ-MgO layer pairs from 5.5 to 10.5 as shown in Fig. 7.29 (top). The experimentally obtained single layer thicknesses of the 5.5 and 10.5 pair structure are given in the caption and show smaller variation compared to the MgO–ZnO structure of Fig. 7.28. Indeed, the SNMS isotope intensity depth profile

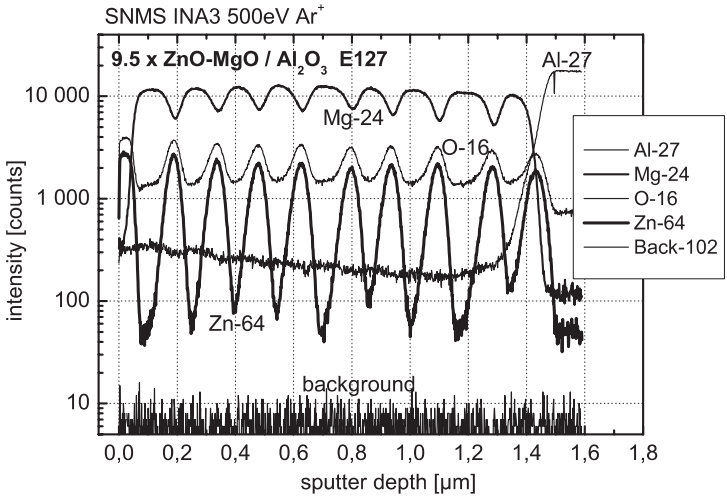


**Fig. 7.28.** SNMS isotope intensity depth profile of a 9.5 pair ZnO-MgO Bragg mirror grown by PLD on *c*-plane sapphire. This particular Bragg structure had a maximum reflectivity of 85% at 2.3 eV photon energy [94]. The single layer thicknesses obtained from UV–vis ellipsometry varied from 80–96 nm (MgO) and 41–71 nm (ZnO)

in Fig. 7.29 (bottom) shows improved lateral thickness homogeneity of the 5.5 pair Bragg structure as expressed by the considerably improved isotope intensity oscillations. First potentially suitable laser structures consisting of YSZ/MgO Bragg–ZnO–YSZ/MgO Bragg are currently under test. Furthermore, $ZrO_2$–MgO Bragg mirrors were also deposited by PLD on ZnO nano- and micropillars with diameter in the 1 µm range and a considerable enhancement of the CL intensity from the pillar was detected [96].

First results on growth and optical investigation of ZnO quantum well layers embedded in MgZnO with higher band gap energy as future light emitters are shown in Fig. 7.30 [53]. Because the surface roughness $R_a$ of the first MgZnO layer was in the 3 nm range, the actual structure of the thinnest quantum wells with nominal thickness of 3 nm is not clear up to now. It could be more a spike-like structure of isolated ZnO dots rather than a closed 2D-like layer, as imaged by AFM in [53]. Nevertheless, Fig. 7.30 shows a remarkable blue-shift coupled with intensity enhancement of the excitonic ZnO peak by decreasing the nominal ZnO quantum well thickness from 25 nm down to 3 nm. The combination of blueshift and increasing intensity are a clear indication for optical confinement of the excitons.

### 7.5.3 Schottky Diodes to ZnO Thin Films

The application of capacitance spectroscopy as for example DLTS (see Sect. 7.4.3 and 7.4.5) requires high-quality Schottky contacts to ZnO single

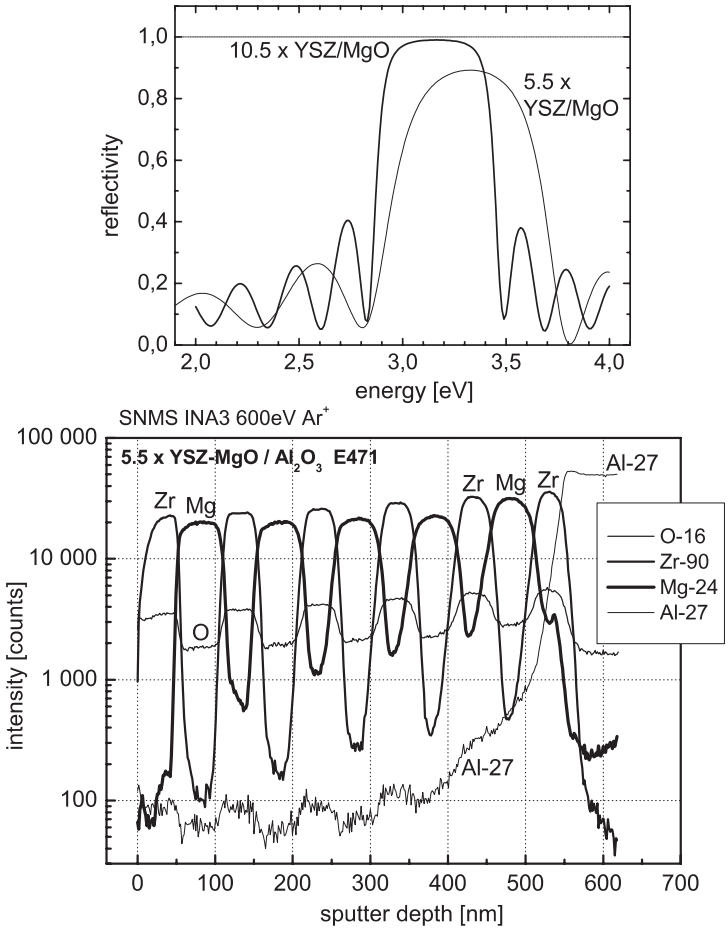


**Fig. 7.29.** *Top*: Reflectivity at normal incidence of two PLD grown Bragg mirrors with 5.5 and 10.5 YSZ-MgO layer pairs obtained from the ellipsometry model analysis. By doubling the layer number, the reflectivity was increased from 90 to 99%. The UV–vis ellipsometry data were fitted best with layer thicknesses of 38–46 nm YSZ/48–54 nm MgO for the 5.5 layer pair Bragg, and $46.4 \pm 0.7$ nm YSZ and $51.9 \pm 0.5$ nm MgO for the 10.5 pair Bragg. Measured and calculated by R. Schmidt-Grund. *Bottom*: SNMS isotope intensity depth profile of this $5.5 \times$ YSZ/MgO Bragg structure

crystals and thin films. Furthermore, because of the current difficulties to reproducibly obtain highly p-type conducting ZnO, Schottky contacts represent an alternative route to devices with rectifying electrical properties. Continuous improvement of the surface preparation technique prior to the evaporation of the Schottky contact metal, comparison of different Schottky contact metals [60], the introduction of the innovative front-to-back Schottky

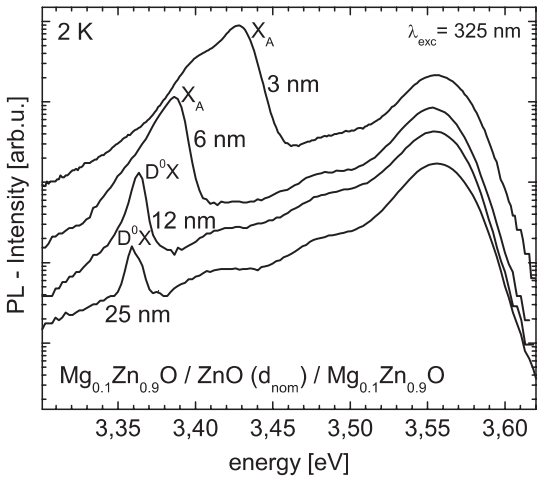


**Fig. 7.30.** Photoluminescence spectra (2K) of PLD MgZnO-ZnO-MgZnO quantum well heterostructures on sapphire with nominal thickness of the ZnO quantum well of 25, 12, 6, and 3 nm [53]. The blueshift of the excitonic peak combined with the intensity enhancement is a clear indication of optical confinement in the ZnO layer

diode configuration with ohmic back contact ZnO:Al layer below the undoped or doped ZnO layer as already mentioned in Sect. 7.4.5 resulted in good Schottky contacts on PLD ZnO thin films [55, 57]. On the insulating sapphire substrate, at first an about 50 nm thick highly Al-doped ZnO film was deposited that serves as the ohmic back contact. On top of this back contact layer, the nominally undoped or doped ZnO films are grown. The ZnO:Al films are contacted with sputtered Au film. The Pd Schottky contacts were realized by thermal evaporation of Pd through shadow masks. The contact area is usually around $10^{-4}$ cm$^2$. The series resistance of such front-to-back Pd–ZnO–ZnO:Al–Au Schottky diodes is as low as about 50–200 Ω [55].

Figure 7.31 demonstrates the very good rectifying behavior of such a Pd Schottky diode on undoped ZnO thin film. The current density ratio determined for bias voltages of +0.6 V and –3 V is about $10^4$ as shown in the inset of Fig. 7.31. The ideality factor $n$ is about 1.5. The temperature-dependent current–voltage (IV, see Fig. 7.31) and capacitance–voltage (CV) measurements from 210 to 300 K explain the reason for the slight deviation of the ideality factor from unity and the dependence of the reverse current on the reverse bias. The barrier heights of the diode of Fig. 7.31 $\Phi_{IV}$ and $\Phi_{CV}$ as determined from IV- and CV-measurements amount to 0.82 and 1.16 eV, respectively [97]. The difference of the two barrier height values is due to the different effect of lateral potential fluctuations as explained in detail in [55, 57, 97].

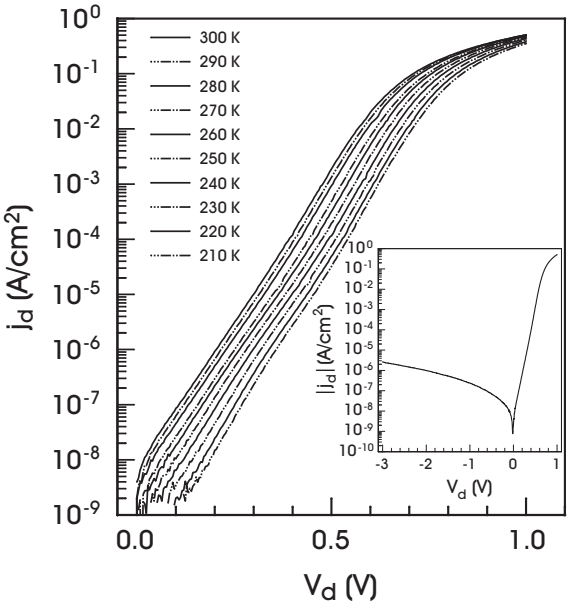


**Fig. 7.31.** Superior rectifying behavior of a Pd Schottky contact on PLD ZnO film with ohmic ZnO:Al back layer contact, with excellent stability at different temperature. The *inset* shows the current density–voltage dependence for a larger voltage range at 290 K. Reprinted with permission from [55]

### 7.5.4 PLD of ZnO pn-Junctions, First LEDs, and Other Highlights

Table 7.10 gives an overview on selected highlights of the PLD of ZnO thin films, thereby demonstrating the state of the art. The table is divided into three sections, corresponding to (1) p-type ZnO films and pn-junctions, (2) n-type ZnO and MgZnO films on various substrate materials, and (3) ferromagnetic 3d-element doped ZnO films. For the results of the Leipzig group see Table 7.9. The following results in Table 7.10 should be especially emphasized: (a) the p-type ZnO films and the ZnO-LED structure grown by laser MBE of semiconductor-quality ZnO films on lattice matched $ScAlMgO_4$ (SCAM) single crystals by the group of M. Kawasaki at Tohuku University Sendai in Japan, (b) the systematic PLD of ZnO and MgZnO films for solar blind photodetectors in the group of T. Venkatesan at University of Maryland in the U.S.A., and (c) the PLD-based systematics on ferromagnetic 3d-element doped ZnO by J. M. D. Coey at Trinity College, University of Dublin, Ireland. For a recent review on p-type doping of ZnO including a list of published p-type films and their deposition technique and devices see also the review [43]. For more general reviews on ZnO covering results from all deposition techniques see [41, 42, 44, 45], and also [98].

**Table 7.10.** Selected highlights of the PLD of (1) p-type ZnO films, including pn-junctions, (2) n-type ZnO films on various substrates, and (3) ferromagnetic films

| Keyword | ZnO-based structure, methods, state of the art result | Refs. |
|---|---|---|
| p-type ZnO:N films | Temperature-modulation epitaxy of atomically smooth p-ZnO:N/i-ZnO/n-ZnO/buffer-ZnO on SCAM by laser MBE with $p = 2 \times 10^{16}\,\mathrm{cm}^{-3}$ ($c_\mathrm{N} = 2 \times 10^{20}\,\mathrm{cm}^{-3}$), $\mu_\mathrm{H} = 8\,\mathrm{cm}^2\,(\mathrm{V\,s})^{-1}$ (300 K), and $N_\mathrm{D}/N_\mathrm{A} = 0.8$ ($E_\mathrm{A} = 100\,\mathrm{meV}$) | [99] |
| ZnO LED | ZnO-based LED with pn-junction and electroluminescence with maxima around 3.05 eV (405 nm) and 2.15 eV with 20 mA injection current | [99] |
| ZnO:P films | doping behavior of PLD ZnO:P($1 - 5$ at. %) films, after annealing semi-insulating films by deep level formation | [100] |
| p-ZnO:As films | PLD of ZnO together with As from effusion cell, p-type proved by Hall effect: $p = 8 \times 10^{16}$ to $4 \times 10^{17}\,\mathrm{cm}^{-3}$, and $\mu = 6$–$35\,\mathrm{cm}^2\,(\mathrm{V\,s})^{-1}$, growth also on GaAs | [101] |
| ZnO LED | Au/p(i)-ZnO/n-ZnO single crystal/In structure grown by $N_2O$ plasma enhanced PLD, rectifying behavior, bluish-white electroluminescence | [102] |
| p-NiO/ n-ZnO junction | ZnO/NiO/ITO on (111)YSZ grown by PLD, p-type NiO:Li(10 at. %) annealed, rectifying behavior in dependence on UV illumination, UV sensing properties | [103] |
| $Zn_3P_2$/ n-ZnO diode | PLD of ZnO and $Zn_3P_2$ on sapphire(0001), laser annealing of the $Zn_3P_2$, rectifying behavior | [104] |
| n-ZnO on SCAM | Laser-MBE of high-quality n-type ZnO and MgZnO films on SCAM grown at 950°C and $10^{-7}$ mbar, $\mu_\mathrm{H} = 440\,\mathrm{cm}^2\,(\mathrm{V\,s})^{-1}$ (300 K) and 5,000 $\mathrm{cm}^2\,(\mathrm{V\,s})^{-1}$ (100 K), effect of $Mg_xZn_{1-x}O$ capping layers on the PL of ZnO/SCAM | [105, 106] |
| n-ZnO on GaN | PLD of high-quality ZnO and GaN on *c*-plane sapphire, enhanced CL excitonic intensity compared to ZnO/sapphire | [107] |
| n-ZnO on $SrTiO_3$ | PLD of undoped and Al-doped ZnO(11-20) on $SrTiO_3$(001) and (011), structure, field effect experiments (FET) | [108–110] |
| n-ZnO on InP | Surface morphology evolution of PLD ZnO films on InP(100) at 623 K growth temperature | [111] |
| n-ZnO on $Al_2O_3$ | PLD/laser MBE of ZnO on *c*-plane sapphire, structure and electrical properties in dependence on oxygen pressure and growth temperature, optical properties, properties of A, B, C exciton, band gap and strain for ZnO on *c*- and *r*-plane sapphire, and fused silica | [112–116] |

**Table 7.10.** (continued)

| Keyword | ZnO-based structure, methods, state of the art result | Refs. |
|---|---|---|
| Polarity controlled ZnO | Laser MBE of Zn-face and O-face ZnO films on ZnO(0001) single crystals, Zn-face shows $R_a = 0.18$ nm, $R_{rms} = 0.21$ nm and $R_{peak-valley} = 0.74$ nm. | [117] |
| MgZnO | PLD of $Mg_xZn_{1-x}O$ ($0 \leq x \leq 1$) in wurtzite and cubic phase, solar blind photodetectors | [118, 119] |
| ZnO:3d-elements | Room temperature ferromagnetism found in PLD (110)ZnO:Sc, Ti, V, Fe, Co, Ni thin films on $r$-plane sapphire, but not for ZnO:Cr, Mn, Cu (all 5 at. %). Large moments of 1,9 and 0.5 $\mu_B$/atom for ZnO:Co and ZnO:Ti, respectively | [120, 121] |
| Mn–Zn–O films | Origin of ferromagnetism in low-temperature processed ZnO:Mn is probably oxygen vacancy stabilized $Mn_{2-x}Zn_xO_{3-\delta}$ | [122], see also [123] |

Compare also the PLD review [22]. For results of the Leipzig group see Table 7.9

## 7.6 Advanced PLD Techniques

In this section advanced developments of the PLD technique are shortly described, e.g., the combinatorial approach and laser MBE. Because of the increasing research interest in ZnO-based nanostructures, the established PLD (at background gas pressure $10^{-4}-3$ mbar) was extended to much higher pressures of 50–200 mbar to grow arrays of free-standing ZnO nanowires. This unique high-pressure PLD process allows the growth of ZnO-based nanostructures with controlled shape and diameter and excellent optical properties.

### 7.6.1 Advances in PLD of Thin Films

The flexibility of the PLD caused by decoupling of laser and growth chamber promoted the development of a variety of advanced PLD techniques to open new growth possibilities and to overcome some limitations of the technique. Table 7.11 gives an overview on recent advances in PLD of thin films. The PLD with ps- or ns-pulse length lasers and the pulsed electron beam deposition (PED) developed by Neocera refer to advanced pulsed energy sources for plasma generation. The PED process uses a pulsed electron beam gun instead of the expensive excimer laser and has therefore high potential to push the application of the technique towards commercial deposition. The other advanced PLD techniques modify the deposition conditions (laser MBE) or the geometric arrangement in multitarget deposition (combinatorial and gradient approaches) in order to ensure cleaner nucleation and deposition under UHV conditions or simultaneous deposition of composition libraries of new multielement compounds. For such libraries, appropriate characterization tools with high lateral resolution are necessary to benefit from the fast

**Table 7.11.** Advanced techniques for the PLD of thin films

| PLD technique | Main innovation, advantages | References |
|---|---|---|
| PLD with sub-ns pulse length laser | Comparison fs-laser to ns-laser: higher kinetic energy of ablated ZnO species, higher mosaicity, smaller grain size, but also smaller residual stress of ZnO on *c*-sapphire. May be advantageous for special materials | [124, 125] |
| Continuous composition spread (CCS-PLD) | Continuous, controlled, vertical composition gradient by PLD, for example, applied for $Ba_{1-x}Sr_xTiO_3$ films | [126–128] |
| Combinatorial PLD | Dramatic increase of the rate of discovery and improvement of new compounds, synthesis of up to thousands of different compositions on one wafer in a single growth run | [129–131] |
| PLD in UHV (laser-MBE) | MBE-like background pressure and in situ RHEED to ensure clean and controlled deposition of high-quality nucleation layers and films. For particular systems as $SrTiO_3$ and $BaTiO_3$, atomically smooth surface and interface were obtained | [128, 132] |
| RF- and ion-beam assisted PLD | PLD chamber equipped with RF or microwave plasma source or ion beam source to enhance the composition of particular film components such as N or O to grow in-plane aligned films on polycrystalline substrates, and to grow nanostructures | [128] |
| Off-axis and dual laser PLD for droplet reduction | Dynamic melt studies of the target surface, time synchronized irradiation of the target with $CO_2$ and KrF lasers leads to particulate free ZnO films | [133, 134] |
| PLD for series production | Pilot scale production PLD systems are in successful operation for X-ray mirrors and are commercially available with excellent thickness and composition homogeneity and reproducibility | [14, 128] |
| Pulsed electron beam deposition (PED) | Pulsed electron beam source emitting 100 ns long electron pulses with 10–20 keV and ∼kA intensity into the deposition chamber, no excimer laser is required, innovative complimentary technique to PLD, further extending the range of materials to be grown as thin films by pulsed energy techniques | [128, 135] |

and cost effective deposition of complete mixing range materials by combinatorial PLD. Furthermore, hybrid techniques are used employing additional lasers, RF or microwave (ECR) plasma sources, or ion beam sources to modify the target ablation for droplet suppression or to improve film composition and structure. Thus, Table 7.11 summarizes the innovative potential that is inherent to PLD.

### 7.6.2 High-Pressure PLD of ZnO-Based Nanostructures

Only a few attempts to obtain nanostructured Si and ZnO using PLD have been published in the last years [136–139]. Figure 7.32 shows the scheme of the high-pressure PLD chamber specially designed for nano-heterostructures using a T-shaped quartz tube with an outer diameter of 30 mm in the Leipzig group [140]. A KrF excimer laser beam enters along the center of the T and is focused on the cylindrical surface of one of the two rotating laser targets, thus allowing in situ modulation of chemical composition of the grown nanostructures. The laser energy density on the target is about $2\,\mathrm{J\,cm^{-2}}$, which is similar to conventional PLD film growth conditions. An encapsulated heater with an arrangement of KANTHAL wire in ceramic tubes and FIBROTHAL isolation material is built around the T-shape quartz tube. The growth temperature is usually chosen between 500 and 950°C as measured by a thermocouple. A downstream gas flow of argon of $0.05$–$0.2\,\mathrm{l\,min^{-1}}$ results in an Ar gas pressure from 25 to 200 mbar. The diameter of single ZnO wires could be varied between about 50 and 3,000 nm by control of the target to substrate distance from 5 to 35 mm [140]. The *a*-plane or *c*-plane sapphire

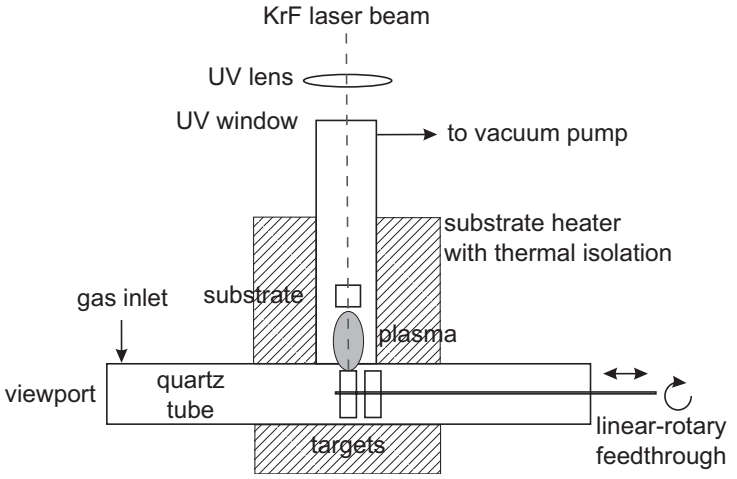


**Fig. 7.32.** Schematic illustration of the high-pressure PLD chamber for ZnO-based nano-heterostructures consisting of a T-shaped quartz tube with 30 mm outer diameter. Reprinted with permission from [140]

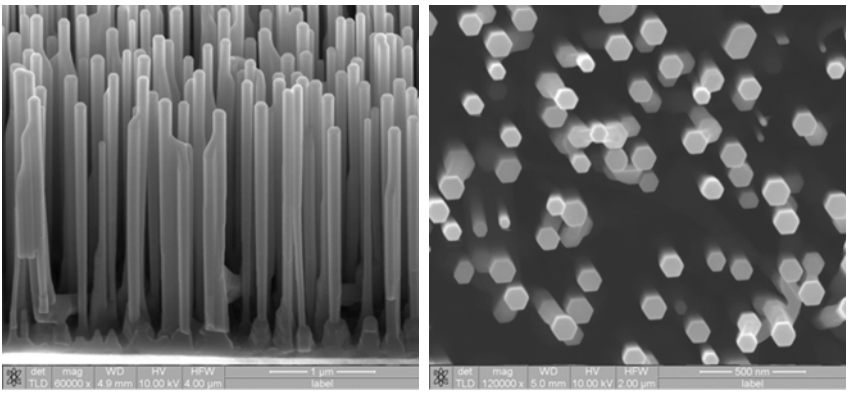

**Fig. 7.33.** Typical SEM images of PLD grown ZnO nanowires (100 mbar Ar, 840°C) on *a*-plane sapphire with Au colloides as nucleation sites [142]

substrates (size $1 \times 1\,\mathrm{cm}^2$) were arranged off-axis, i.e., parallel to the expanding plasma plume. They were partially (using a hole mask) or fully covered before PLD with DC-sputtered gold films of nominally 1 nm thickness. Alternatively, gold colloides of variable size and lateral density or laterally aligned gold seeds obtained by nanosphere lithography mask transfer technique [141] can be used as growth templates. Typical SEM images of ZnO nanowires grown by high-pressure PLD at 100 mbar Ar pressure and at 840°C on *a*-plane sapphire covered with Au colloides are shown in Fig. 7.33 [142].

## 7.7 Summary

This chapter about pulsed laser deposition demonstrated the extensive opportunities of PLD to grow nominally undoped and doped ZnO thin films and heterostructures with well defined structure, surface morphology, and electrical and optical properties. An outstanding advantage of PLD in comparison to other physical and chemical growth techniques is the flexibility in doping and alloying ZnO thin films with a variety of dopant elements and oxides, thus making PLD most suitable for exploratory research on new materials. Furthermore, because PLD is especially appropriate for all kind of oxides, multilayer heterostructures can be easily built from different oxide materials by PLD.

PLD ZnO thin films grown at higher temperature of a few 100°C are usually crystalline and granular with minimum average and rms surface roughness down to 0.2 nm. For selected materials and growth conditions, atomically smooth film surfaces were also obtained. The grains show a nearly perfect, single crystal-like vertical and lateral alignment on various single crystalline substrates as $ScAlMgO_4$ (SCAM), *c*- and *a*-plane sapphire, and GaN. The combination of ZnO with dielectric and ferroelectric materials

($SrTiO_3$, $BaTiO_3$) with fixed and switchable polarization, respectively, offers new perspectives for innovative electronic and storage devices. The carrier concentration of n-type conducting PLD ZnO thin films can be controlled from highly doped $10^{20}\,cm^{-3}$ down to the semi-insulating $10^{12}\,cm^{-3}$ range. The electron mobility of PLD ZnO films on sapphire and SCAM exceeds 150 and $300\,cm^2\,(V\,s)^{-1}$ at room temperature, respectively. The peak width of the donor bound exciton peak in low-temperature photoluminescence of high-quality PLD ZnO films is around 1 meV, which is as narrow as measured for commercial ZnO bulk single crystals.

First successful ZnO device demonstrations as for example stable homo- and heteroepitaxial pn-junctions and LED structures, thin film scintillators, and quantum well structures with optical confinement, and oxide-based Bragg reflectors, and high-quality Schottky contacts are based on PLD grown thin films. Several techniques as for example the PLD in UHV conditions (laser MBE), and gradient and combinatorial PLD, and high-pressure PLD for nano-heterostructures show the innovative potential of the advanced growth technique PLD.

*Acknowledgement.* The author thanks all colleagues of the Semiconductor Physics Group of University Leipzig for their kind cooperation in the scientific and technical preparation of this manuscript, especially for providing graphs of published and unpublished results and for help on LaTeX. These PLD developments would not have been possible without the longstanding technical coworkers of the PLD lab Dieter Natusch, Holger Hochmuth and Gabriele Ramm.

The PLD equipment and the initial development of the Leipzig PLD group was financed mainly by the German Federal Ministry of Education and Research (BMBF) from 1990 to 2003 and by the Saxonian Ministry of Science and Art SMWK in Dresden, which is hereby highly acknowledged. Currently, the development of the high-pressure PLD process is supported within the DFG research group 522 "Architecture of nano- and microdimensional building blocks" and by the European Commission within the STREP collaboration project "Nanophotonic and Nanoelectronic Devices from Oxide Semiconductors" NANDOS. The growth of the magnetic ZnO-based films and multilayers is supported by the BMBF Young Scientists group "Nanospintronics."

## References

1. J.T. Cheung, History and Fundamentals of Pulsed Laser Deposition. In: *Pulsed Laser Deposition of Thin Films*, ed. by D.B. Chrisey, G.H. Hubler (Wiley, New York Chichester Brisbane Toronto Singapore 1994) pp 1–22
2. D. Bäuerle, Laser Chemical Processing. In: *Landolt-Börnstein New Series, Group VIII Advanced Materials and Technologies, Vol. 1 Laser Physics and Applications, Subvolume C Laser Applications*, ed. by R. Poprawe, H. Weber, G. Herziger (Springer, Berlin 2004) pp 311–354
3. G.W. Martin, L.A. Doyle, A. Al-Kateeb, I. Weaver, D. Riley, M.J. Lamb, T. Morrow, C.L.S. Lewis, Appl. Surf. Sci. **127–129**, 710 (1998)

4. A. Husmann, Pulsed Laser Deposition mittels gütegeschalteter $CO_2$-Laser. PhD Thesis, RWTH Aachen, Aachen (1999)
5. T. Venkatesan, Pulsed Laser Deposition - Future Trends. In: *Pulsed Laser Deposition of Thin Films*, ed. by D.B. Chrisey, G.H. Hubler (Wiley, New York Chichester Brisbane Toronto Singapore 1994) pp 313–326
6. J.S. Horwitz, Film Nucleation and Film Growth in Pulsed Laser Deposition of Ceramics. In: *Pulsed Laser Deposition of Thin Films*, ed. by D.B. Chrisey, G.H. Hubler (Wiley, New York Chichester Brisbane Toronto Singapore 1994) pp 229–254
7. M. Lorenz, S. Becker, H.-J. Dietze, W. Schmitz, B. Brunner, K.F. Renk, Physica C **182**, 114 (1991)
8. M. Lorenz, H. Hochmuth, D. Natusch, M. Kusunoki, V.L. Svetchnikov, V. Riede, I. Stanca, G. Kästner, D. Hesse, IEEE Trans. Appl. Supercond. **11**, 3209 (2001)
9. J.A. Greer, Commercial Scale-Up of Pulsed Laser Deposition. In: *Pulsed Laser Deposition of Thin Films*, ed. by D.B. Chrisey, G.H. Hubler (Wiley, New York Chichester Brisbane Toronto Singapore 1994) pp 293–312
10. M. Lorenz, H. Hochmuth, D. Natusch, H. Börner, K. Kreher, W. Schmitz, Appl. Phys. Lett. **68**, 3332 (1996)
11. J.S. Horwitz, D.B. Chrisey, R.M. Stroud, A.C. Carter, J. Kim, W. Chang, J.M. Pond, S.W. Kirchoefer, M.S. Osofsky, D. Koller, Appl. Surf. Sci. **127–129**, 507 (1998)
12. D. Bäuerle, *Laser Processing and Chemistry*, 3rd edn. (Springer, Berlin Heidelberg Newyork, 2000), pp 3–100
13. L.A. Doyle, G.W. Martin, A. Al-Kateeb, I. Weaver, D. Riley, M.J. Lamb, T. Morrow, C.L.S. Lewis, Appl. Surf. Sci. **127–129**, 716 (1998)
14. Applied X-ray Optics AXO Dresden GmbH, Heidenau, Germany, http://www.axo-dresden.de
15. AxynTeC Dünnschichttechnik GmbH, Augsburg, Germany, http://www.axyntec.de
16. nanovation SARL, Orsay, France, http://www.nanovation.biz
17. B. Angstenberger, Fliehkraftunterstütztes Laserbeschichten. PhD Thesis, Universität Stuttgart, Stuttgart (2000)
18. E.W. Kreutz, Appl. Surf. Sci. **127–129**, 606 (1998)
19. K.L. Saenger, Angular Distribution of Ablated Material. In: *Pulsed Laser Deposition of Thin Films*, ed. by D.B. Chrisey, G.H. Hubler (Wiley, New York Chichester Brisbane Toronto Singapore 1994) pp 199–228
20. L.-C. Chen, Particulates Generated by Pulsed Laser Ablation. In: *Pulsed Laser Deposition of Thin Films*, ed. by D.B. Chrisey, G.H. Hubler (Wiley, New York Chichester Brisbane Toronto Singapore 1994) pp 167–198
21. A.E. Tselev, Cross-beam pulsed laser deposition as a method for preparation of thin films of metastable solid solutions. PhD Thesis, TU Dresden, Dresden (2000)
22. A. Ohtomo, A. Tsukazaki, Semicond. Sci. Technol. **20**, S1 (2005)
23. D.B. Geohegan, Diagnostics and Characteristics of Laser-Produced Plasmas. In: *Pulsed Laser Deposition of Thin Films*, ed. by D.B. Chrisey, G.H. Hubler (Wiley, New York Chichester Brisbane Toronto Singapore 1994) pp 115–166
24. H. Hügel, F. Dausinger, Fundamentals of Laser-Induced Processes. In: *Landolt-Börnstein New Series, Group VIII Advanced Materials and Technologies, Vol. 1 Laser Physics and Applications, Subvolume C Laser Applications*,

ed by R. Poprawe, H. Weber, G. Herziger (Springer, Berlin Heidelberg New York 2004) pp 311–354
25. J. Gottmann, Dynamik der Schichtabscheidung von Keramiken mit KrF-Excimer-Laserstrahlung. PhD Thesis, RWTH Aachen, Aachen (2001)
26. R. Kelly, A. Miotello, Mechanisms of Pulsed Laser Sputtering. In: *Pulsed Laser Deposition of Thin Films*, ed. by D.B. Chrisey, G.H. Hubler (Wiley, New York Chichester Brisbane Toronto Singapore 1994) pp 55–88
27. S.R. Foltyn, Surface Modification of Materials by Cumulative Laser Irradiation. In: *Pulsed Laser Deposition of Thin Films*, ed. by D.B. Chrisey, G.H. Hubler (Wiley, New York Chichester Brisbane Toronto Singapore 1994) pp. 89–114
28. R.E. Leuchtner, Appl. Surf. Sci. **127–129**, 626 (1998)
29. Y. Kawaguchi, A. Narazaki, T. Sato, H. Niino, A. Yabe, Appl. Surf. Sci. **197–198**, 268 (2002)
30. S. Metev, Process Characteristics and Film Properties in Pulsed Laser Deposition. In: *Pulsed Laser Deposition of Thin Films*, ed. by D.B. Chrisey, G.H. Hubler (Wiley, New York Chichester Brisbane Toronto Singapore 1994) pp 229–254
31. S. Ohashi, M. Lippmaa, N. Nakagawa, H. Nagasawa, H. Koinuma, M. Kawasaki, Rev. Sci. Instrum. **70**, 178 (1999)
32. Information sheet LPX300i Series 1996 and 2004, Coherent Lambda Physik GmbH, Göttingen, Germany, http://www.lambdaphysik.com
33. Information sheet YG980 Pulsed Nd:YAG Laser Specifications, http://www.quantel.fr/uk/, for more details see http://www.bigskylaser.0com/pdf/yg980web.pdf
34. Neocera Inc., Beltsville, MD, U.S.A., http://www.neocera.com
35. Twente Solid State Technology B.V., Hengelo, Netherlands, http://www.tsst.nl
36. Koinuma-Kawasaki Mobile Combinatorial PLD, Huntington Mechanical Laboratories Inc, Mountain View, CA, U.S.A., http://www.huntvac.com/PLD/
37. PVD Products Inc., Wilmington, MA, U.S.A., http://www.pvdproducts.com
38. Surface, Hückelhofen, Germany, http://www.surface-tec.com
39. DCA instruments Oy, Turku, Finland, http://www.dca.fi
40. Pascal Technologies Inc., Fredericksburg, VA, U.S.A., http://www.pascaltechnologies.com
41. Ü. Özgür, Ya. Alivov, C. Liu, A. Teke, M.A. Reshchikov, S. Dogan, V. Avrutin, S.-J. Cho, H. Morkoç, J. Appl. Phys. **98**, 041301 (2005)
42. R. Tribulet, J. Perrière, Prog. Cryst. Growth Charact. Mater. **47**, 65 (2003)
43. D.C. Look, B. Claflin, Phys. Stat. Sol. B **241**, 624 (2004)
44. C. Liu, F. Yun, H. Morkoç, J. Mater. Sci. **16**, 555 (2005)
45. T. Yao, Zinc Oxide. In: *Encyclopedia of Materials: Science and Technology*, (Elsevier, Amsterdam London 2001) pp 9883–9888
46. W. Hirschwald, P. Bonasewicz, L. Ernst, M. Grade, D. Hoffmann, S. Krebs, R. Littbarski, G. Neumann, M. Grunze, D. Kolb, H.J. Schulz, Zinc Oxide. In: *Current Topics in Materials Science, Vol. 7*, ed. by E. Kaldis (North Holland, Amsterdam 1981) pp 143–482
47. A. Rahm, High-resolution X-ray diffraction of ZnO-based thin films. Diploma thesis, Universität Leipzig, Leipzig (2003)

48. M. Lorenz, H. Hochmuth, H. von Wenckstern, H. Schmid, W. Mader, M. Grundmann, Crystalline nanostructure of PLD ZnO and MgZnO thin films on sapphire. In: *Universität Leipzig, The Physics Institutes Report 2004*, ed. by M. Grundmann (Leipzig 2005) p 156
49. S. Heitsch, C. Bundesmann, G. Wagner, G. Zimmermann, A. Rahm, H. Hochmuth, G. Benndorf, H. Schmidt, M. Schubert, M. Lorenz, H. Schmidt, M. Schubert, M. Grundmann, Thin Solid Films **496**, 234 (2006)
50. M. Lorenz, H. Hochmuth, A. Jammoul, G. Ferro, C. Förster, J. Pezoldt, J. Zuniga Perez, G. Benndorf, J. Lenzner, R. Schmidt-Grund, M. Grundmann, Wissenschaftlich-Technische Berichte of Research Center Rossendorf **FZR-433**, 74 (2005)
51. E.M. Kaidashev, M. Lorenz, H. von Wenckstern, A. Rahm, H.-C. Semmelhack, K.-H. Han, G. Benndorf, C. Bundesmann, H. Hochmuth, M. Grundmann, Appl. Phys. Lett. **82**, 3901 (2003)
52. Y.F. Chen, D.M. Bagnall, H. Koh, K. Park, K. Hiraga, Z. Zhu, T. Yao, J. Appl. Phys. **84**, 3912 (1998)
53. S. Heitsch, G. Benndorf, G. Zimmermann, C. Schulz, D. Spemann, H. Hochmuth, H. Schmidt, Th. Nobis, M. Lorenz, M. Grundmann, Appl. Phys. A **88**, 99 (2007)
54. M. Lorenz, H. Hochmuth, J. Lenzner, M. Brandt, H. von Wenckstern, G. Benndorf, M. Grundmann, Wissenschaftlich-Technische Berichte of Research Center Rossendorf **FZR-433**, 57 (2005)
55. M. Grundmann, H. von Wenckstern, R. Pickenhain, Th. Nobis, A. Rahm, M. Lorenz, Superlatt. Microstruct. **38**, 317 (2005)
56. M. Lorenz, E.M. Kaidashev, H. von Wenckstern, V. Riede, C. Bundesmann, D. Spemann, G. Benndorf, H. Hochmuth, A. Rahm, H.-C. Semmelhack, M. Grund mann, Solid State Electron. **47**, 2205 (2003)
57. H. von Wenckstern, S. Weinhold, G. Biehne, R. Pickenhain, H. Schmidt, H. Hochmuth, M. Grundmann, Donor Levels in ZnO. In: *Advances in Solid State Physics, Vol. 45*, ed. by B. Kramer (Springer, Berlin Heidelberg New York 2005) pp 263–275
58. H. von Wenckstern, G. Benndorf, S. Heitsch, J. Sann, M. Brandt, H. Schmidt, J. Lenzner, M. Lorenz, A.Y. Kuznetsov, B.K. Meyer, M. Grundmann, Appl. Phys. A **88**, 125 (2007)
59. H. von Wenckstern, M. Brandt, H. Schmidt, G. Biehne, R. Pickenhain, H. Hochmuth, M. Lorenz, M. Grundmann, Appl. Phys. A **88**, 135 (2007)
60. H. von Wenckstern, E.M. Kaidashev, M. Lorenz, H. Hochmuth, G. Biehne, J. Lenzner, V. Gottschalch, R. Pickenhain, M. Grundmann, Appl. Phys. Lett. **84**, 79 (2004)
61. M. Grundmann, H. von Wenckstern, Proc. FVS-Workshop TCOs für Dünnschichtsolarzellen und andere Anwendungen, Freyburg, Germany, 10–12. April 2005, Hahn–Meitner–Institut Berlin
62. B.K. Meyer, H. Alves, D.M. Hofmann, W. Kriegseis, D. Forster, F. Bertram, J. Christen, A. Hoffmann, M. Straburg, M. Dworzak, U. Haboeck, A.V. Rodina, Phys. Stat. Sol. B **241**, 231 (2004)
63. W. Czakai, Photolumineszenz an ZnO. Diploma thesis, Universität Leipzig, Leipzig (2004)
64. M. Strassburg, A. Rodina, M. Dworzak, U. Haboeck, I.L. Krestnikov, A. Hoffmann, O. Gelhausen, M.R. Phillips, H.R. Alves, A. Zeuner, D.M. Hofmann, B.K. Meyer, Phys. Stat. Sol. B **241**, 607 (2004)

65. D. Spemann, E.M. Kaidashev, M. Lorenz, J. Vogt, T. Butz, Nucl. Instrum. Meth. B **219–220**, 891 (2004)
66. C. Bundesmann, M. Schubert, D. Spemann, T. Butz, M. Lorenz, E.M. Kaidashev, M. Grundmann, N. Ashkenov, H. Neumann, G. Wagner, Appl. Phys. Lett. **81**, 2376 (2002)
67. C. Bundesmann, M. Schubert, D. Spemann, A. Rahm, H. Hochmuth, M. Lorenz, M. Grundmann, Appl. Phys. Lett. **85**, 905 (2004)
68. C. Bundesmann, A. Rahm, M. Lorenz, M. Grundmann, M. Schubert, J. Appl. Phys. **99**, 113504 (2006)
69. R. Schmidt, B. Rheinländer, M. Schubert, D. Spemann, T. Butz, J. Lenzner, E.M. Kaidashev, M. Lorenz, M. Grundmann, Appl. Phys. Lett. **82**, 2260 (2003)
70. R. Schmidt-Grund, M. Schubert, B. Rheinländer, D. Fritsch, H. Schmidt, E.M. Kaidashev, M. Lorenz, C.M. Herzinger, M. Grundmann, Thin Solid Films **455–456**, 500 (2004)
71. R. Schmidt-Grund, A. Carstens, B. Rheinländer, D. Spemann, H. Hochmut, G. Zimmermann, M. Lorenz, M. Grundmann, C.M. Herzinger, M. Schubert, J. Appl. Phys. **99**, 123701 (2006)
72. J. Zuniga-Perez, V. Munoz-Sanjose, M. Lorenz, G. Benndorf, S. Heitsch, D. Spemann, M. Grundmann, J. Appl. Phys. **99**, 023514 (2006)
73. J. Zuniga Perez, V. Munoz-Sanjose, M. Lorenz, H. Hochmuth, G. Benndorf, S. Heitsch, D. Spemann, M. Grundmann, Third SOXESS workshop on ZnO, EC Contract G5RT-CT-2002-05075, 28 September – 1 October 2005, Gallipoli, Italy, Poster p.13
74. C. Bundesmann, N. Ashkenov, M. Schubert, D. Spemann, T. Butz, E.M. Kaidashev, M. Lorenz, M. Grundmann, Appl. Phys. Lett. **83**, 1974 (2003)
75. S. Heitsch, Photoluminescence of p-doped ZnO thin films. M.Sc. thesis, Universität Leipzig, Leipzig (2003)
76. H. von Wenckstern, S. Heitsch, G. Benndorf, D. Spemann, E.M. Kaidashev, M. Lorenz, M. Grundmann, AIP Conf. Proc. **772**, 183 (2005)
77. M. Diaconu, H. Schmidt, H. Hochmuth, M. Lorenz, G. Benndorf, J. Lenzner, D. Spemann, A. Setzer, K.-W. Nielsen, P. Esquinazi, M. Grundmann, Thin Solid Films **486**, 117 (2005)
78. H. Schmidt, M. Diaconu, H. Hochmuth, M. Lorenz, A. Setzer, P. Esquinazi, A. Pöppl, D. Spemann, K.W. Nielsen, R. Gross, G. Wagner, M. Grundmann, Superlatt. Microstruct. **39**, 334 (2006)
79. M. Diaconu, H. Schmidt, A. Pöppl, R. Böttcher, J. Hoentsch, A. Klunker, D. Spemann, H. Hochmuth, M. Lorenz, M. Grundmann, Phys. Rev. B **72**, 085214 (2005)
80. M. Diaconu, H. Schmidt, A. Pöppl, R. Böttcher, J. Hoentsch, A. Rahm, H. Hochmuth, M. Lorenz M. Grundmann, Superlatt. Microstruct. **38**, 413 (2005)
81. H. Schmidt, M. Diaconu, H. Hochmuth, G. Benndorf, H. von Wenckstern, G. Biehne, M. Lorenz, M. Grundmann, Appl. Phys. A **88**, 157 (2007)
82. M. Diaconu, H. Schmidt, H. Hochmuth, M. Lorenz, H. von Wenckstern, G. Biehne, M. Grundmann, Solid State Commun. **137**, 417 (2006)
83. Qingyu Xu, L. Hartmann, H. Schmidt, H. Hochmuth, M. Lorenz, R. Schmidt-Grund, D. Spemann, A. Rahm, M. Grundmann, Thin Solid Films **515**, 2549 (2006)

84. Qingyu Xu, L. Hartmann, H. Schmidt, H. Hochmuth, M. Lorenz, R. Schmidt-Grund, C. Sturm, D. Spemann, M. Grundmann, Phys. Rev. B **73**, 205342 (2006)
85. M. Ungureanu, H. Schmidt, Q.Y. Xu, H. von Wenckstern, D. Spemann, H. Hochmuth, M. Lorenz, M. Grundmann, E-MRS Spring Meeting, Nice, 29 May to 2 June 2006, Symposium K: ZnO and related materials, Poster K PII 02
86. M. Schubert, N. Ashkenov, T. Hofmann, M. Lorenz, H. Hochmuth, H. von Wenckstern, M. Grundmann, G. Wagner, Ann. Phys. (Leipzig) **13**, 61 (2004)
87. N. Ashkenov, M. Schubert, E. Twerdowski, B.N. Mbenkum, H. Hochmuth, M. Lorenz, H.V. Wenckstern, W. Grill, M. Grundmann, Thin Solid Films **486**, 153 (2005)
88. B.N. Mbenkum, N. Ashkenov, M. Schubert, M. Lorenz, H. Hochmuth, D. Michel, M. Grundmann, G. Wagner, Appl. Phys. Lett. **86**, 091904 (2005)
89. M. Lorenz, H. Hochmuth, J. Lenzner, T. Nobis, G. Zimmermann, M. Diaconu, H. Schmidt, H. von Wenckstern, M. Grundmann, Thin Solid Films **486**, 205 (2005)
90. R. Johne, M. Lorenz, H. Hochmuth, J. Lenzner, H. von Wenckstern, G. Zimmermann, H. Schmidt, R. Schmidt-Grund, M. Grundmann, Appl. Phys. A **88**, 89 (2007)
91. W.W. Moses, Nucl. Instrum. Meth. A **487**, 123 (2002)
92. S.E. Derenzo, M.J. Weber, E. Bourret-Courchesne, M.K. Klintenberg, Nucl. Instrum. Meth. A **505**, 111 (2003)
93. R. Johne, Kathodolumineszenz-Untersuchung von ZnO-Dünnfilmen für Szintillator-Anwendungen - Experiment und Modellierung. Diploma thesis, Universität Leipzig, Leipzig (2006)
94. M. Lorenz, H. Hochmuth, R. Schmidt-Grund, E.M. Kaidashev, M. Grundmann, Ann. Phys.(Leipzig) **13**, 59 (2004)
95. R. Schmidt-Grund, T. Nobis, V. Gottschalch, B. Rheinländer, H. Herrnberger, M. Grundmann, Thin Solid Films **483**, 257 (2005)
96. R. Schmidt-Grund, T. Gühne, H. Hochmuth, B. Rheinländer, A. Rahm, V. Gottschalch, J. Lenzner, M. Grundmann, SPIE **6038**, 489 (2006)
97. H. von Wenckstern, G. Biehne, R. Abdel Rahman, H. Hochmuth, M. Lorenz, M. Grundmann, Appl. Phys. Lett. **88**, 092102 (2006)
98. C. Klingshirn, M. Grundmann, A. Hoffmann, B. Meyer, A. Waag, Phys. J. **5**, 33 (2006)
99. A. Tsukazaki, A. Ohtomo, T. Onuma, M. Ohtani, T. Makino, M. Sumiya, K. Ohtani, S.F. Chichibu, S. Fuke, Y. Segawa, H. Ohno, H. Koinuma, M. Kawasaki, Nat. Mater. **4**, 2 (2005)
100. Y.-W. Heo, S.J. Park, K. Ip, S.J. Pearton, D.P. Norton, Appl. Phys. Lett. **83**, 1128 (2003)
101. Y.R. Ryu, T.S. Lee, H.W. White, Appl. Phys. Lett. **83**, 87 (2003)
102. X.-L Guo, J.-H. Choi, H. Tabata, T. Kawai, Jpn. J. Appl. Phys. **40**, L177 (2001)
103. H. Ohta, M. Hirano, K. Nakahara, K. Nakahara, H. Maruta, T. Tanabe, M. Kamiya, T. Kamiya, H. Hosono, Appl. Phys. Lett. **83**, 1029 (2003)
104. S.Y. Lee, E.S. Shim, H.S. Kang, S.S. Pang, J.S. Kang, Thin Solid Films **473**, 31 (2005)
105. T. Makino, K. Tamura, C.H. Chia, Y. Segawa, M. Kawasaki, A. Ohtomo, H. Koinuma, Appl. Phys. Lett. **81**, 2172 (2002)

106. A. Tsukazaki, A. Ohtomo, M. Kawasaki, Appl. Phys. Lett. **88**, 152106 (2006)
107. R.D. Vispute, V. Talyansky, S. Choopun, R.P. Sharma, T. Venkatesan, M. He, X. Tang, J.B. Halpern, M.G. Spencer, Y.X. Li, L.G. Salamanca-Riba, A.A. Iliadis, K.A. Jones, Appl. Phys. Lett. **73**, 348 (1998)
108. E. Bellingeri, D. Marre, I. Pallecchi, L. Pellegrino, A.S. Siri, Appl. Phys. Lett. **86**, 012109 (2005)
109. E. Bellingeri, D. Marre, I. Pallecchi, L. Pellegrino, G. Canu, A.S. Siri, Thin Solid Films **486**, 186 (2005)
110. M. Karger, M. Schilling, Phys. Rev. B **71**, 075304 (2005)
111. E. Vasco, C. Zaldo, L. Vazquez, J. Phys.: Condens. Mat. **13**, L663 (2001)
112. S. Choopun, R.D. Vispute, W. Noch, A. Balsamo, R.P. Sharma, T. Venkatesan, A. Iliadis, D.C. Look, Appl. Phys. Lett. **75**, 3947 (1999)
113. X.W. Sun, H.S. Kwok, J. Appl. Phys. **86**, 408 (1999)
114. A. Ohtomo, H. Kimura, K. Saito, T. Makino, Y. Segawa, H. Koinuma, M. Kawasaki, J. Cryst. Growth **214–215**, 284 (2000)
115. J.F. Muth, R.M. Kolbas, A.K. Sharma, J. Appl. Phys. **85**, 7884 (1999)
116. V. Srikant, D.R. Clarke, J. Appl. Phys. **81**, 6357 (1997)
117. H. Matsui, H. Saeki, T. Kawai, A. Sasaki, M. Yoshimoto, M. Tsubaki, H. Tabata, J. Vac. Sci. Technol. B **22**, 2454 (2004)
118. S. Choopun, R.D. Vispute, W. Yang, R.P. Sharma, T. Venkatesan, Appl. Phys. Lett. **80**, 1529 (2002)
119. R.D. Vispute, S.S. Hullavarad, D.E. Pugel, V.N. Kulkarni, S. Dhar, I. Takeuchi, T. Venkatesan, Wide band gap ZnO and MgZnO heterostructures for future optoelectronic devices. In: *Thin Films and Heterostructures for Oxide Electronics*, ed. by S.B. Ogale (Springer, Berlin Heidelberg New York 2005) pp 301–330
120. M. Venkatesan, C.B. Fitzgerald, J.G. Lunney, J.M.D. Coey, Phys. Rev. Lett. **93**, 177206 (2004)
121. A.K. Pradhan, K. Zhang, S. Mohanty, J.B. Dadson, D. Hunter, J. Zhang, D.J. Sellmyer, U.N. Roy, Y. Cui, A. Burger, S. Mathews, B. Joseph, B.R. Sekhar, B.K. Roul, Appl. Phys. Lett. **86**, 152511 (2005)
122. D.C. Kundaliya, S.B. Ogale, S.E. Lofland, S. Dhar, C.J. Metting, S.R. Shinde, Z. Ma, B. Varughese, K.V. Ramanujachary, L. Salamanca-Riba, T. Venkatesan, Nat. Mater. **3**, 709 (2004)
123. S.J. Pearton, W.H. Heo, M. Ivill, D.P. Norton, T. Steiner, Semicond. Sci. Technol. **19**, R59 (2004)
124. J. Perriere, E. Millon, W. Seiler, C. Boulmer-Leborgne, V. Cracium, O. Albert, J.C. Loulergue, J. Etchepare, J. Appl. Phys. **91**, 690 (2002)
125. M. Okoshi, K. Higashikawa, M. Hanabusa, Jpn. J. Appl. Phys. **40**, 1287 (2001)
126. H.M. Christen, S.D. Silliman, K.S. Harshavardhan, Rev. Sci. Instrum. **72**, 2673 (2001); & ORNL-CMSD progress report **ORNL-6969**, 76 (2002)
127. X. Zhu, H.L.-W. Chan, C.-L. Choy, K.H. Wong, D. Hesse, J. Appl. Phys. **97**, 093503 (2005)
128. T. Venkatesan, K.S. Harshavardhan, M. Strikovski, J. Kim, Recent advances in the deposition of multi-component oxide films by pulsed energy deposition. In: *Thin Films and Heterostructures for Oxide Electronics*, ed. by S.B. Ogale (Springer, Berlin Heidelberg New York 2005) pp 385–413
129. I. Takeuchi, Combinatorial synthesis of functional materials. In: *Thin Films and Heterostructures for Oxide Electronics*, ed. by S.B. Ogale (Springer, Berlin Heidelberg New York 2005) pp 333–352

130. Z. Jin, T. Fukumura, M. Kawasaki, K. Ando, H. Saito, T. Sekiguchi, Y.Z. Yoo, M. Mukarami, Y. Matsumoto, T. Hasegawa, H. Koinuma, Appl. Phys. Lett. **78**, 3824 (2001)
131. Z.W. Jin, Y.Z. Yoo, T. Sekiguchi, T. Chikyow, H. Ofuchi, H. Fujioka, M. Oshima, H. Koinuma, Appl. Phys. Lett. **83**, 39 (2003)
132. A. Tsukazaki, A. Ohtomo, T. Kita, Y. Ohno, H. Ohno, M. Kawasaki, Science **315**, 1388 (2007) & K. Ueda, H. Tabata, T. Kawai, Science **280**, 1064 (1998)
133. M. Siegert, W. Zander, J. Lisoni, J. Schubert, C. Buchal, Appl. Phys. A **69**, S 779 (1999)
134. P. Mukherjee, S. Chen, J.B. Cuff, P. Sakthivel, S. Witanachchi, J. Appl. Phys. **91**, 1828 (2002)
135. M. Strikovski, K.S. Harshavardhan, Appl. Phys. Lett. **82**, 853 (2003)
136. A.M. Morales, C.M. Lieber, Science **279**, 208 (1998)
137. Y.H. Tang, Y.F. Zhang, N. Wang, I. Bello, C.S. Lee, S.T. Lee, J. Appl. Phys. **85**, 7981 (1999)
138. M. Kawakami, A.B. Hartando, Y. Nakata, T. Okada, Jpn. J. Appl. Phys. **42**, L33 (2003)
139. M. Yan, H.T. Zhang, E.J. Widjaja, R.P.H. Chang, J. Appl. Phys. **94**, 5240 (2003)
140. M. Lorenz, E.M. Kaidashev, A. Rahm, Th. Nobis, J. Lenzner, G. Wagner, D. Spemann, H. Hochmuth, M. Grundmann, Appl. Phys. Lett. **86**, 143113 (2005)
141. A. Rahm, M. Lorenz, T. Nobis, G. Zimmermann, M. Grundmann, B. Fuhrmann, F. Syrowatka, Appl. Phys. A **88**, 31 (2007)
142. A. Rahm, T. Nobis, M. Lorenz, G. Zimmermann, N. Boukos, A. Travlos, M. Grundmann, Adv. Solid State Phys. **46**, in press (2007)